

**Postsynaptic GluA3 subunits are required for appropriate assembly of AMPA receptor
GluA2 and GluA4 subunits on mammalian cochlear afferent synapses and for
presynaptic ribbon modiolar-pillar morphological distinctions**

Mark A. Rutherford¹, Atri Bhattacharyya¹, Maolei Xiao¹, Hou Ming Cai², Indra Pal², María E.
Rubio^{2,3*}

1.Department of Otolaryngology, Washington University School of Medicine, St. Louis, MO
63110

2.Department of Neurobiology, University of Pittsburgh School of Medicine, Pittsburgh, PA
15261

3.Department of Otolaryngology, University of Pittsburgh School of Medicine, Pittsburgh, PA
15261

Running title: GluA3 is essential for the molecular anatomy of cochlear ribbon synapses

Keywords: glutamate receptors, ultrastructure; qRT-PCR; immunolabeling; inner hear cells; 3D
reconstructions; confocal imaging

Number of text pages: 57

Number of Figures: 9

Number of words for Abstract: 244

Number of words for Introduction: 851

Number of words for Discussion: 2,373

Number of additional files: 11 (3 supplemental figures; 8 supplemental source data files)

*Corresponding Author:

María Eulalia Rubio: Mer@pitt.edu

Department of Neurobiology; University of Pittsburgh Medical School

BST3 Building, 3501 Fifth Avenue #10016, Pittsburgh, PA 15261

Impact Statement

Ultrastructural and imaging studies of cochlear ribbon synapses demonstrate cis- and trans-synaptic molecular and structural effects in the absence of the AMPA-type glutamate receptor subunit GluA3 during mouse development in ambient sound levels.

Acknowledgments

This work was supported by NIDCD DC013048 (MER) and NIDCD DC14712 (MAR). We thank Nicholas Lozier for his helpful comments on the manuscript.

Authors' contributions: M.E.R and M.A.R.: designed research, performed research, analyzed data and wrote and edited the manuscript. M.X. and H.M.C.: performed research and edited the manuscript. A.B. and I.P.: analyzed data and edited the manuscript.

The authors declare no competing financial interests.

Abstract

Cochlear sound encoding depends on α -amino-3-hydroxy-5-methyl-4-isoxazole propionic acid receptors (AMPA), but reliance on specific pore-forming subunits is unknown. With 5-week-old male C57BL/6J *Gria3* knockout mice (i.e., subunit GluA3^{KO}) we determined cochlear function, synapse ultrastructure and AMPAR molecular anatomy at ribbon synapses between inner hair cells (IHCs) and spiral ganglion neurons. GluA3^{KO} and wild-type (GluA3^{WT}) mice reared in ambient sound pressure level (SPL) of 55-75 dB had similar auditory brainstem response (ABR) thresholds, wave-1 amplitudes and latencies. Postsynaptic densities (PSDs), presynaptic ribbons, and synaptic vesicle sizes were all larger on the modiolar side of the IHCs from GluA3^{WT}, but not GluA3^{KO}, demonstrating GluA3 is required for modiolar-pillar synapse differentiation. Presynaptic ribbons juxtaposed with postsynaptic GluA2/4 subunits were similar in quantity, however, lone ribbons were more frequent in GluA3^{KO} and GluA2-lacking synapses were observed only in GluA3^{KO}. GluA2 and GluA4 immunofluorescence volumes were smaller on the pillar side than the modiolar side in GluA3^{KO}, despite increased pillar-side PSD size. Overall, the fluorescent puncta volumes of GluA2 and GluA4 were smaller in GluA3^{KO} than GluA3^{WT}. However, GluA3^{KO} contained less GluA2 and greater GluA4 immunofluorescence intensity relative to GluA3^{WT} (3-fold greater mean GluA4:GluA2 ratio). Thus, GluA3 is essential in development, as germline disruption of *Gria3* caused anatomical synapse pathology before cochlear output became symptomatic by ABR. We propose the hearing loss in older male GluA3^{KO} mice results from progressive synaptopathy evident in 5-week-old mice as decreased abundance of GluA2 subunits and an increase in GluA2-lacking, GluA4-monomeric Ca²⁺-permeable AMPARs.

Introduction

In the cochlea and ascending central auditory system, hearing relies on fast excitatory synaptic transmission via unique α -amino-3-hydroxy-5-methyl-4-isoxazolepropionic acid receptors (AMPA_Rs) (Raman et al., 1994; Ruel et al., 1999; Gardner et al., 1999; Glowatzki and Fuchs, 2002). AMPA_Rs are tetrameric ionotropic receptor-channels comprised of GluA1-4 pore-forming subunits plus auxiliary subunits conferring distinct electrophysiological kinetics, unique molecular structures, and different pharmacological sensitivities (Jackson et al., 2011; Bowie, 2018; Azumaya et al., 2017; Twomey et al., 2018). In the adult brain, most AMPA_R tetramers contain an RNA-edited form of the GluA2 subunit that makes the channel relatively impermeable to Ca^{2+} , resulting in Ca^{2+} -impermeable AMPA_Rs (CI-AMPA_Rs; Sommer et al., 1991; Higuchi et al., 1993). AMPA_Rs lacking edited GluA2 are called Ca^{2+} -permeable AMPA_Rs (CP-AMPA_Rs) because they have greater permeability to Ca^{2+} and larger overall ionic conductance, carried mainly by Na^{+} (Hollmann et al., 1991; Geiger et al., 1995). The expression of GluA2-lacking CP-AMPA_Rs is downregulated in the developing brain (Pickard et al., 2000; Kumar et al., 2002; Henley and Wilkinson, 2016). However, CP-AMPA_Rs persist or even increase with developmental maturation in some neurons of the auditory brainstem where CP-AMPA_Rs enriched in GluA3 and GluA4 subunits are thought to be essential for fast transmission of acoustic signals (Trussell, 1997; Gardner et al., 2001; Lawrence and Trussell, 2000; Sugden et al., 2002; Wang and Manis, 2005; Youssoufian et al., 2005; Luján et al., 2019).

Cochlear afferent projections process fast auditory signals through innervation of the anteroventral cochlear nucleus, at the endbulb of Held synapses onto bushy cells, where the AMPA_Rs are comprised mainly of GluA3 and GluA4 subunits with high Ca^{2+} permeability and rapid desensitization kinetics (Wang et al., 1998; Rubio et al., 2017). Mice lacking the GluA3 subunit have impaired auditory processing due to effects on synaptic transmission associated with altered ultrastructure of synapses between endbulbs and bushy cells (García-Hernández et

al., 2017; Antunes et al., 2020). Mice lacking the GluA4 subunit have altered acoustic startle responses and impaired transmission at the next synaptic relay at the calyx of Held in the brainstem, a high-fidelity central synapse (Yang et al., 2011; García-Hernández and Rubio, 2022). The rapid processing of auditory signals in the brainstem is supported by high-fidelity initial encoding of sound at peripheral synapses between cochlear inner hair cells (IHCs) and spiral ganglion neurons (SGNs) (Rutherford and Moser, 2016; Rutherford et al., 2021), however, relatively little is known about how synapse ultrastructure, molecular composition, and overall abundance of cochlear AMPARs depends on specific pore-forming subunits.

In mice, the developmental onset of hearing function begins at the end of the 2nd postnatal week, followed by activity-dependent maturation and neuronal diversification that depends on glutamatergic transmission in the SGNs (Shrestha et al., 2018; Sun et al., 2018; Petitpre et al., 2018; 2022). Heterogeneity of the SGNs and the ribbon synapses driving them results in auditory nerve fibers with mutually diverse sound response properties correlated to differences in synapse structure and position of innervation on the IHC modiolar-pillar axis (Merchán-Perez and Liberman, 1996; Ohn et al., 2016). Each primary auditory nerve fiber (i.e., type-I SGN) is unbranched and driven to fire spikes by the release of glutamate from an individual IHC ribbon synapse driving a single, large post-synaptic density (PSD) of approximately 850 nm in length, on average (cat: Liberman, 1980; mouse Payne et al., 2021). In the mature cochlea, the PSD is populated with AMPARs comprised of subunits GluA2-4 but not GluA1 (Niedzielski and Wenthold, 1995; Matsubara et al., 1996; Parks, 2000; Shrestha et al., 2018). Afferent signaling in the auditory nerve, as well as noise-induced excitotoxicity at cochlear afferent synapses (a form of synaptopathy), depends on activation of AMPARs (Ruel et al., 2000; Hu et al., 2020). However, the dependence of cochlear AMPAR function and pathology on specific pore-forming subunits is unclear.

Here, we examined the influence of GluA3 subunits on afferent synapse ultrastructure and on AMPAR-subunit molecular anatomy in the PSD of the auditory nerve fiber in the mouse cochlea, with attention to GluA2 and GluA4 *flip* and *flop* isoforms and to positions of SGN innervation on the IHC modiolar-pillar axis. At the central auditory nerve projection in the cochlear nucleus, at the endbulb of Held synapse, GluA3 is required for both postsynaptic and presynaptic maturation of synapse structure and function (García-Hernández et al., 2017; Antunes et al., 2020). Therefore, we also examined presynaptic ribbon morphology in relation to position on the IHC modiolar-pillar axis, which is expected to show smaller and more spherical ribbons on the side of the IHC facing the pillar cells and outer hair cells (pillar side) relative to the ribbons on the modiolar side facing the ganglion (Merchán-Perez and Liberman, 1996; Payne et al., 2021). Our findings in young adult male GluA3^{KO} mice include dysregulation of GluA2 and GluA4 subunit relative abundance and alterations in pre- and post-synaptic ultrastructure associated with an increased vulnerability to glutamatergic synaptopathy at ambient, background levels of sound. These structural and molecular alterations at the cochlear ribbon synapses of pre-symptomatic 5-week-old male GluA3^{KO} mice appear to be pathological, preceding the reduction in ABR wave-1 amplitudes observed at 2 months of age (García-Hernández et al., 2017).

Results

Cochlear responses to sound and transcriptional splicing of *Gria2* and *Gria4* mRNA isoforms are similar in 5-week-old GluA3^{WT} and GluA3^{KO} mice.

The four AMPAR pore-forming subunits GluA1-4 are encoded by four genes, *Gria1-4*. Here, we studied mice with normal or disrupted *Gria3* (i.e., GluA3^{WT} or GluA3^{KO}; García-Hernández et al., 2017; Rubio et al., 2017). We first determined whether the 5-week-old C57BL/6J GluA3^{WT} and GluA3^{KO} differed in cochlear responses to sound. Complete statistical details are included in source data files online. Our ABR analysis showed no differences between genotypes in clicks

or pure tone thresholds or wave-1 amplitude or latency (**Figure 1A**). We note that male GluA3^{KO} and GluA3^{WT} mice at two months of age have similar ABR thresholds but GluA3^{KO} mice have reduced ABR wave-1 amplitudes (García-Hernández et al., 2017), suggesting cochlear deafferentation between postnatal weeks 5 and 9.

We then asked if disruption of *Gria3* affected expression of GluA1, GluA2, or GluA4 protein subunits in the cochlear spiral ganglion (the auditory nerve fiber, SGN somata) or the cochlear nucleus (**Figure 1B-C**). In WT mice, mature SGNs express GluA2, GluA3, and GluA4 subunits of the AMPAR, but not GluA1 (Niedzielski and Wenthold, 1995; Matsubara et al., 1996; Parks, 2000; Shrestha et al., 2018). With immunolabelling, we observed GluA2 and GluA4 in the SGNs of both genotypes, and we confirmed that SGNs lacked GluA1 in GluA3^{WT} mice, as expected. Moreover, we did not observe compensatory GluA1 expression in SGNs of GluA3^{KO} (**Figure 1B, left**). We also checked immunolabeling of GluA1 on brainstem sections containing the ventral cochlear nucleus and cerebellum. As expected, we found GluA1 immunoreactivity in the cerebellar Bergmann glia of GluA3^{WT} and GluA3^{KO} mice (Matsui et al., 2005; Douyard et al., 2007). In contrast, the ventral cochlear nucleus of 5-week-old mice lacked GluA1 immunoreactivity in GluA3^{WT} as previously shown (Wang et al., 1998). Also similar to the SGNs, we found no compensational expression of GluA1 in neurons of the cochlear nucleus from GluA3^{KO} mice (**Figure1B, right**). At ribbon synapses in the cochlea, the PSDs on the postsynaptic terminals of SGNs expressed GluA2, 3, and 4 in GluA3^{WT} as previously shown (Sebe et al., 2017), while PSDs in GluA3^{KO} lacked specific immunolabeling for GluA3 (**Figure 2**). This confirmed the deletion of GluA3 subunits was effective in SGNs of GluA3^{KO} mice, as previously shown in the cochlear nucleus (García-Hernández et al., 2017; Rubio et al., 2017), and was not associated with compensatory upregulation of GluA1 subunits.

Two unique isoforms termed *flip* and *flop* are generated by alternative splicing of the mRNA encoding each of the pore-forming GluA subunits. In the brain, *flip* and *flop* splice variants are expressed in distinct but partly overlapping patterns and impart different desensitization kinetics (Sommer et al., 1990). The chicken and rat cochlear nuclei express predominantly the fast-desensitizing *flop* isoforms (Schmid et al., 2001; Sugden et al., 2002). With qRT-PCR, we determined whether *Gria3* disruption altered posttranscriptional *flip* and *flop* splicing of mRNA for GluA2 (*Gria2* gene) or GluA4 (*Gria4* gene) in the cochlea. We measured the levels of *flip* or *flop* for *Gria2* and *Gria4* mRNA and compared GluA3^{WT} to GluA3^{KO} (**Figure 1C**). Although GluA3^{KO} exhibited increased variance in transcript abundance among samples for all four isoforms and a trend toward greater mRNA abundance in all four comparisons, we found no significant differences between GluA3^{KO} and GluA3^{WT}. In addition, we calculated the *flip/flop* ratios for *Gria2* and *Gria4* in GluA3^{WT} and GluA3^{KO} and found no differences between genotype (*Gria2* *flip/flop* ratio WT: 0.67 ± 0.02 , GluA3^{KO}: 0.67 ± 0.01 ; $p = 0.8$; *Gria4* *flip/flop* ratio, WT: 0.70 ± 0.001 , GluA3^{KO}: 0.70 ± 0.01 , $p = 0.9$, paired t-test two-tailed).

Thus, *Gria3* disruption did not affect hearing sensitivity at 5-weeks of age, in contrast to 8-weeks of age when ABR peak amplitudes were reduced (García-Hernández et al., 2017). Taken together with previous work, this suggests the 5-week-old GluA3^{KO} cochlea may be in a pathological but pre-symptomatic, vulnerable state. The levels of *Gria2* or *Gria4* *flip* or *flop* mRNA isoforms in cochleae of male mice at 5-weeks of age were similar in GluA3^{WT} and GluA3^{KO}. In both genotypes, expression of *Gria2* and *Gria4* *flop* isoforms appeared to exceed expression of the *flip* isoforms.

Pre- and post-synaptic ultrastructural features of Inner Hair Cell ribbon synapses are disrupted in the organ of Corti of GluA3^{KO} mice.

Given the similarity of cochlear responses to sound measured by ABR in male GluA3^{WT} and GluA3^{KO} mice at 5-weeks of age, we next asked if the ultrastructure of IHC-ribbon synapses was similar as well. Qualitatively, in GluA3^{WT} and GluA3^{KO} the general structure and cellular components of the sensory epithelia were similar to published data of C57BL/6 mice (not shown; Ohlemiller and Gagnon, 2004). Synapses from the mid-cochlea of both GluA3^{WT} and GluA3^{KO} mice had electron-dense pre- and post-synaptic membrane specializations and membrane-associated presynaptic ribbons (**Figures 3-4**).

Ultrastructure in C57BL/6 GluA3^{WT}

A total of 29 synapses of GluA3^{WT} mice were analyzed in three dimensions (3D) using serial sections (on average, 7 ultrathin sections per PSD). Of this total, 17 were on the modiolar side and 12 on the pillar side of the IHCs (**Figure 3A-B, Figure 3-figure supplement 1**). In our sample of the modiolar-side synapses, 11 had one single ribbon whereas 6 had two ribbons, so for the analysis of the PSD we classified the synapses as modiolar-1 and modiolar-2, for single and double ribbons respectively. All the pillar-side synapses analyzed had a single ribbon. We then compared the PSD surface area and volume among the synapses of modiolar-1, modiolar-2, and pillar sides. One-way ANOVA comparison of the PSD surface area was significant ($p = 0.007$). Pairwise comparisons showed that the PSD surface areas were similar ($p = 0.98$) for single-ribbon and double-ribbon synapses of the modiolar side (modiolar-1 mean = $0.52 \pm 0.15 \mu\text{m}^2$; modiolar-2 mean = $0.56 \pm 0.15 \mu\text{m}^2$). However, in C57BL/6 WT mice, we observed that PSD surface area was larger for modiolar-side synapses compared to pillar-side synapses ($p = 0.014$ modiolar-1 vs. pillar, and $p = 0.03$ modiolar-2 vs. pillar; pillar mean: $0.40 \pm 0.06 \mu\text{m}^2$) (**Figure 3C, left**). We then measured PSD volumes, which were ~2x larger on the modiolar side, on average, but not significantly different ($p = 0.051$ one-way ANOVA), (modiolar-1 mean = $0.010 \pm 0.006 \mu\text{m}^3$; modiolar-2 mean = $0.008 \pm 0.004 \mu\text{m}^3$; pillar mean = $0.005 \pm 0.002 \mu\text{m}^3$) (**Figure 3C, left**). One-way ANOVA of the PSD linear length showed no significant differences

among synapse type ($p = 0.17$; modiolar-1, $n = 21$; mean length: 666 ± 186 nm; modiolar-2, $n = 6$; mean length: 709 ± 234 nm; pillar, $n = 16$; mean length: 572 ± 135 nm) (**Figure 3D, left**). Overall, our analysis shows the PSD surface areas of modiolar-side synapses are significantly larger than those of the pillar side in GluA3^{WT} on C57BL/6 background.

Presynaptic ribbon volume of GluA3^{WT} was similar between modiolar-side and pillar-side synapses ($p = 0.57$; modiolar mean: 0.0029 ± 0.001 μm^3 , pillar mean: 0.0023 ± 0.0009 μm^3 ; Mann-Whitney U Test, two-tailed) (**Figure 3C, right**). In contrast, the surface area of modiolar-side ribbons was found significantly larger ($p = 0.002$; modiolar mean: 0.141 ± 0.123 μm^2 , pillar mean: 0.074 ± 0.02 μm^2 ; Mann-Whitney U Test, two-tailed) (**Figure 3C, right**). For all pairwise statistical comparisons of ultrastructure in the following, we used the two-tailed Mann-Whitney U Test.

The analyses of the major ribbon axis and shape of GluA3^{WT} showed that the IHC-synapses on the modiolar side had longer major ribbon axes ($p < 0.0001$; mean: 274 ± 75 nm) and less circularity ($p < 0.0001$; mean: 0.51 ± 0.12) compared to the pillar-side ribbons (mean major axes: 180 ± 54 nm; mean circularity: 0.9 ± 0.06). These data show that ribbons on the modiolar side of GluA3^{WT} IHCs are elongated, while those on the pillar side are more round in shape (**Figure 3D, center**), as previously shown for C57BL/6 mice at 5-weeks of age (Payne et al., 2021). Analysis of SV size showed that the SVs of modiolar-side synapses were larger ($p = 0.0029$) than those of the pillar-side synapses (modiolar mean: 36 ± 3 nm; pillar mean: 33 ± 4 nm; **Figure 3D, right**). In summary, GluA3^{WT} synapses of the modiolar side had larger PSD surface areas, more elongated and less circular ribbons, with greater surface area, and larger SVs compared with synapses of the pillar side.

Ultrastructure in C57BL/6 GluA3^{KO}

From GluA3^{KO}, a total of 26 synapses were analyzed in 3D with serial sections (on average, 7 ultrathin sections per PSD). Of this total, 16 were on the modiolar side and 10 on the pillar side of the IHCs (**Figure 4A-B, Figure 4-figure supplement 1**). As with synapses from GluA3^{WT}, for the analysis of the PSDs of GluA3^{KO} we classified the modiolar-side synapses as modiolar-1 (single ribbon; n = 11) or modiolar-2 (double ribbons; n = 5). In contrast to the pillar-side synapses of GluA3^{WT} that had only single ribbons, we found two pillar-side synapses of GluA3^{KO} cochleae with double ribbons (e.g., **Figure 4-figure supplement 1**). These pillar-side synapses with double ribbons were not included in our analysis. We then compared the PSD surface areas and volumes among synapses on the modiolar (modiolar-1, modiolar-2) and pillar sides. One-way ANOVA comparison of the PSD surface area was not significant ($p = 0.67$; modiolar-1 mean: $0.51 \pm 0.18 \mu\text{m}^2$; modiolar-2 mean: $0.55 \pm 0.14 \mu\text{m}^2$; pillar mean: $0.57 \pm 0.16 \mu\text{m}^2$). One-way ANOVA analysis of the PSD volume was not significant ($p = 0.65$; modiolar-1 mean: $0.0085 \pm 0.004 \mu\text{m}^3$; modiolar-2 mean: $0.0068 \pm 0.001 \mu\text{m}^3$; pillar mean: $0.0083 \pm 0.003 \mu\text{m}^3$) (**Figure 4C, left**). The PSD linear lengths were not significantly different ($p = 0.07$, one-way ANOVA; modiolar-1, n = 30, mean length: $629 \pm 147 \text{ nm}$; modiolar-2, n = 6, mean length: $543 \pm 32 \text{ nm}$; pillar, n = 17, mean length: $684 \pm 118 \text{ nm}$) (**Figure 4D, left**).

Analysis of GluA3^{KO} presynaptic ribbon volumes showed that pillar-side synapses (mean: $0.0042 \pm 0.001 \mu\text{m}^3$) had larger volumes than modiolar-side synapses (mean: $0.0032 \pm 0.001 \mu\text{m}^3$; $p = 0.047$) (**Figure 4C, right**), in contrast to GluA3^{WT}. However, unlike GluA3^{WT}, the surface area was similar between ribbons on the modiolar and pillar sides of GluA3^{KO} (modiolar mean: $0.14 \pm 0.14 \mu\text{m}^2$, pillar mean: $0.17 \pm 0.25 \mu\text{m}^2$; $p = 0.91$) (**Figure 4C, right**).

The major ribbon axes from GluA3^{KO} were similar on the modiolar-side (mean: $199 \pm 65 \text{ nm}$) and pillar-side (mean: $201 \pm 89 \text{ nm}$; $p = 0.9$). Modiolar-side ribbons had less circularity than pillar -side ribbons (modiolar mean: 0.75 ± 0.10 ; pillar mean: 0.85 ± 0.07 ; $p = 0.01$) (**Figure 4D,**

right), but this difference was lesser than the difference observed in GluA3^{WT}. Opposite to the pattern in GluA3^{WT}, SVs of modiolar-side synapses were smaller than those of the pillar side in GluA3^{KO} (modiolar: 35 ± 5 nm; pillar: 38 ± 3 nm; $p = 0.04$) (**Figure 4D, right**). In summary, unlike GluA3^{WT}, GluA3^{KO} synapses of the modiolar side had similar PSD and ribbon surface areas and ribbon long-axes as pillar-side synapses, and smaller SVs, demonstrating disruption of modiolar-pillar synaptic differentiation during development.

Inner Hair Cell modiolar-pillar differences are eliminated or reversed in GluA3^{KO}.

We then compared PSDs and ribbons among GluA3^{WT} and GluA3^{KO} mice on the modiolar and pillar sides (**Figure 5A**). Overall, the PSD surface area and volume of the modiolar-side synapses (modiolar-1 and modiolar-2) were similar between genotypes (surface area: $p = 0.85$; volume: $p = 0.62$; one-way ANOVA). In contrast, the mean surface area and volume of the pillar-side PSDs was larger in GluA3^{KO} than GluA3^{WT} (surface area: $p = 0.013$; volume $p = 0.007$) (**Figure 5A, top**). The average PSD length was similar between genotypes for the modiolar-side synapses ($p = 0.29$, one-way ANOVA). In contrast, the PSD length of GluA3^{KO} pillar-side synapses was larger than GluA3^{WT} ($p = 0.02$) (**Figure 5B, top**).

Synaptic ribbon volumes differed among modiolar and pillar groups of GluA3^{WT} and GluA3^{KO} ($p = 0.04$, one-way ANOVA). Pairwise comparisons showed that ribbon volumes of modiolar-side synapses were similar between GluA3^{WT} and GluA3^{KO} ($p = 0.93$). In contrast, the pillar-side synapses were larger in GluA3^{KO} than in GluA3^{WT} ($p = 0.03$) (**Figure 5A, bottom**). One-way ANOVA of the analysis of the ribbon surface area between modiolar-side and pillar-side synapses was similar between GluA3^{WT} and GluA3^{KO} ($p = 0.39$) (**Figure 5A, bottom**).

Differences between the ribbon major axis were found between GluA3^{WT} and GluA3^{KO} ($p < 0.0001$, one-way ANOVA). On the modiolar side, analysis of the ribbon major axis length

showed that those of the GluA3^{KO} were significantly smaller than GluA3^{WT} ($p < 0.0001$), whereas pillar-side synapses were similar in major axis length ($p = 0.82$) (**Figure 5B, bottom left**). Differences in ribbon circularity were also found between genotypes ($p < 0.0001$, one-way ANOVA). Paired comparisons showed that modiolar-side ribbons were significantly less circular in GluA3^{WT} ($p < 0.0001$), whereas pillar-side ribbons were of similar circularity among genotypes ($p = 0.62$) (**Figure 5B, bottom center**). SVs size differed between genotypes ($p = 0.0008$, one-way ANOVA). Data showed that SVs of modiolar-side synapses were similar among genotypes ($p = 0.84$), while those of pillar-side synapses were significantly larger in GluA3^{KO} ($p = 0.0004$) (**Figure 5D, bottom right**).

Altogether, our data of 5-week-old male mice show the AMPAR subunit GluA3 is essential to establish and/or maintain the morphological gradients of presynaptic and postsynaptic structures along the modiolar-pillar axis of the IHC. In GluA3^{KO} enlargement of PSD surface area, presynaptic ribbon size, and synaptic vesicle size on the pillar side eliminated the modiolar-pillar morphological distinctions seen in 5-week-old male GluA3^{WT} mice on C57BL/6 background. Next, we asked how these early ultrastructural changes in GluA3^{KO} correlated with the number of ribbon synapses per IHC and the relative expression of GluA subunits at those synapses.

An increase in GluA2-lacking synapses precedes a reduction in cochlear output in GluA3^{KO} mice.

Although GluA3^{KO} mice have reduced ABR wave-1 amplitudes at 2-months of age (Garcia-Hernandez et al., 2017), they were not yet different from GluA3^{KO} mice at 5-weeks of age (**Figure 1A**). Given the alterations in ribbon synapse ultrastructure at 5-weeks (**Figures 3-5**), we asked if synapse molecular anatomy was also affected in GluA3^{KO} mice. Using confocal images of immunolabeled cochlear wholemounts, we analyzed the expression of CtBP2, GluA2, GluA3,

and GluA4 at the ribbon synapses between IHCs and SGNs. Visual inspection of the images revealed robust anti-GluA3 labeling in GluA3^{WT} and the absence of specific anti-GluA3 labeling in GluA3^{KO}. As well, there was an obvious reduction in GluA2 labeling and increase in GluA4 labeling in GluA3^{KO} relative to GluA3^{WT} (**Figures 2, 6A**). Despite this, the numbers of paired synapses (CtBP2+GluA2+GluA4) per IHC were similar in the whole cochlea (**Figure 6B**; WT: 18.1 ± 2.8 ; KO: 17.3 ± 3.8 ; $p = 0.94$, Mann-Whitney two-tailed U Test) and within apical, middle, and basal cochlear regions (see **Figure 6** caption for more statistical details, Mann-Whitney two-tailed U Test unless otherwise noted). The numbers of ribbonless synapses per IHC (GluA2+GluA4 – WT: 1.2 ± 0.64 ; KO: 1.1 ± 0.59 ; $p = 0.67$) and GluA4-lacking synapses (GluA2+CtBP2 – WT: 0.035 ± 0.044 ; KO: 0.062 ± 0.095 ; $p = 0.81$) were not significantly different. In contrast, the numbers of lone ribbons per IHC (CtBP2-only – WT: 0.97 ± 0.92 ; KO: 1.6 ± 0.84 ; $p = 0.021$) and GluA2-lacking synapses per IHC (GluA4+CtBP2 – WT: 0.0 ± 0.0 ; KO: 0.07 ± 0.09 ; $p = 0.028$) were significantly increased in GluA3^{KO} relative to GluA3^{WT} (**Figure 6B**).

Loss of GluA3 expression reduces synaptic GluA2 and increase synaptic GluA4 subunits.

Grayscale and color images (**Figures 2, 6A**) revealed obvious reduction in GluA2 and increase in GluA4 subunit immunofluorescence per synapse, on average, as quantified in **Figure 7A** ($n = 3$ mid-cochlear images per genotype). The overall GluA fluorescence per synapse ($\text{GluA}_{\text{Sum}} = \text{GluA2} + \text{GluA3} + \text{GluA4}$) tended to be smaller in GluA3^{KO} due to the absence of GluA3 subunit fluorescence. Analysis of GluA2 and GluA4 puncta volumes and intensities in one exemplar mid-cochlear image from GluA3^{WT} and GluA3^{KO} mice revealed that ribbon synapses of GluA3^{KO} mice had more compact AMPAR arrays (**Figure 7B**) with reduced GluA2 and increased GluA4 fluorescence intensity relative to GluA3^{WT} (**Figure 7C**). The sublinear Volume vs. Intensity relationship for each GluA subunit suggests synaptic AMPAR density increases with the size of the GluA array in both genotypes (**Figure 7D**). Data from three mid-cochlear image stacks from

each genotype are summarized in **Figure 7E-H** (same images as panel A). Relative to the mean of the summed pixel intensities per synapse in GluA3^{WT} mice, the overall fluorescence of GluA subunits ($\text{GluA}_{\text{Sum}} = \text{GluA2} + \text{GluA3} + \text{GluA4}$) was reduced in GluA3^{KO} mice due to the absence of GluA3, despite the much larger increase in GluA4 fluorescence intensity relative to the reduction in GluA2 (**Figure 7E-F**). Relative to the mean GluA puncta volume per GluA3^{WT} synapse, the mean volumes of GluA2, GluA4, and GluA_{Sum} were all reduced in GluA3^{KO} (**Figure 7G**). When normalized to the mean puncta volume per image in either group, the distributions of synapse volumes were broadened for GluA2 and GluA4 subunits in GluA3^{KO} relative to GluA3^{WT} (**Figure 7H**). For each image, we calculated the coefficient of variation ($\text{CV} = \text{SD} / \text{mean}$) in puncta volume for comparison by genotype. The volume of GluA_{Sum} had a CV (mean \pm SD, $n = 3$ images per genotype) of 0.38 ± 0.03 in GluA3^{WT} versus 0.51 ± 0.02 in GluA3^{KO}. For GluA2 volumes, the CVs were 0.39 ± 0.03 in GluA3^{WT} versus 0.65 ± 0.065 in GluA3^{KO}. For GluA4 volumes, the CVs were 0.38 ± 0.04 in GluA3^{WT} versus 0.51 ± 0.02 in GluA3^{KO}. Summed pixel intensity per synapse was more variable than volume and, again, more variable in GluA3^{KO} than in GluA3^{WT}. For GluA_{Sum} intensity, the CVs were 0.44 ± 0.04 in GluA3^{WT} versus 0.63 ± 0.02 in GluA3^{KO}. For GluA2 intensity, the CVs were 0.46 ± 0.03 in GluA3^{WT} versus 0.76 ± 0.04 in GluA3^{KO}. For GluA4 intensity, the CVs were 0.45 ± 0.05 in GluA3^{WT} versus 0.63 ± 0.02 in GluA3^{KO}.

To test the statistical significance and to confirm the differences observed in **Figure 7** in a larger data set from a replication cohort, we next assessed mean synaptic CtBP2, GluA2, and GluA4 volume and intensity per image in 14 image stacks from each genotype. In image stacks of sufficient quality, we also measured synapse position on the IHC modiolar-pillar axis to sort synapses into modiolar and pillar groups, dividing them at the midpoint of the range of ribbon centroids in the image Z-axis (**Figure 8-figure supplement 1**). Image means and group means are displayed in **Figure 8**. The volumes of CtBP2, GluA2, and GluA4 puncta were significantly

smaller in GluA3^{KO} relative to GluA3^{WT} (**Figure 8A**, all, in μm^3 ; CtBP2–GluA3^{WT}: 0.14 ± 0.02 ; CtBP2–GluA3^{KO}: 0.12 ± 0.01 , $p = 0.008$; GluA2–GluA3^{WT}: 0.47 ± 0.06 ; GluA2–GluA3^{KO}: 0.39 ± 0.07 , $p = 0.0001$; GluA4–GluA3^{WT}: 0.45 ± 0.05 ; GluA4–GluA3^{KO}: 0.36 ± 0.02 , $p = 4.9 \times 10^{-6}$). When comparing modiolar-side and pillar-side synapse, in both genotypes CtBP2 puncta tended to be larger on the modiolar side than the pillar side, on average, but the differences were not significant ($p = 0.08$ for GluA3^{WT} and GluA3^{KO}). In GluA3^{WT}, GluA2 and GluA4 modiolar-side and pillar-side puncta were not significantly different in volume ($p = 0.42$ GluA2; $p = 0.23$ GluA4). In contrast, in GluA3^{KO}, GluA2 and GluA4 puncta were significantly larger on the modiolar side than the pillar side ($p = 0.001$ GluA2; $p = 0.0001$ GluA4).

When comparing the two genotypes on either the modiolar-sides or the pillar sides (**Figure 8A**, M or P), the group mean volumes tended to be larger in GluA3^{WT} than GluA3^{KO} for CtBP2, GluA2, and GluA4. However, the CtBP2 volumes were not significantly different when comparing genotypes in the anatomical subgroups ($p = 0.098$ for modiolar; $p = 0.57$ for pillar). For GluA2, only the pillar-side groups were significantly different, with a marked reduction in GluA3^{KO} ($0.36 \pm 0.09 \mu\text{m}^3$) relative to GluA3^{WT} ($0.45 \pm 0.06 \mu\text{m}^3$; $p = 0.008$). For GluA4, both the modiolar- and pillar-side synapses were significantly smaller in GluA3^{KO} (M: $0.40 \pm 0.026 \mu\text{m}^3$; P: $0.33 \pm 0.028 \mu\text{m}^3$) relative to GluA3^{WT} (M: $0.49 \pm 0.078 \mu\text{m}^3$, $p = 0.0058$; P: $0.44 \pm 0.055 \mu\text{m}^3$, $p = 0.0004$).

In contrast to mean CtBP2 volume, which was decreased in GluA3^{KO} (**Figure 8A**), median CtBP2 intensity (**Figure 8B**) and density (**Figure 8C**) were significantly increased in GluA3^{KO}. For CtBP2 intensity (a.u.) $\times 10^5$ – GluA3^{WT}: 1.2 ± 0.3 ; GluA3^{KO}: 1.8 ± 0.3 , $p = 0.0001$). As shown in the representative images assessed in Figure 7, GluA2 intensity and volume were both reduced (**Figure 8A-B**), resulting in no change in GluA2 density (**Figure 8C**). For GluA2 intensity (a.u.) $\times 10^5$

– GluA3^{WT}: 1.8 ± 0.4 ; GluA3^{KO}: 1.4 ± 0.3 , $p = 0.01$. While GluA4 intensity increased, volume was reduced (**Figure 8A-B**), resulting in increased GluA4 density (**Figure 8C**). For GluA4 intensity (a.u.)e⁵ – GluA3^{WT}: 1.7 ± 0.6 ; GluA3^{KO}: 4.2 ± 1.2 , $p = 5e^{-6}$. Relative to GluA3^{WT} synapses, the GluA4:GluA2 intensity ratio was 3x greater on average for GluA3^{KO} synapses (**Figure 8D**). For GluA4:GluA2 intensity ratio – GluA3^{WT}: 0.93 ± 0.18 ; GluA3^{KO}: 3.0 ± 0.5 , $p = 6e^{-7}$.

Positive correlations between synaptic puncta volumes, intensities, and sphericities in GluA3^{WT} are reduced in GluA3^{KO} as the range of modiolar-pillar positions is shortened.

In GluA3^{WT}, we commonly observed apparent oscillations in synapse volume as a function of position in the Z-axis of the confocal microscope when the modiolar-pillar dimension was approximately parallel to the Z-axis (**Figure 9A**, left panel, right axis, lower markers). These spatial oscillations were clearer when measured as sphericity (**Figure 9A**, left panel, left axis, upper markers), which was inversely related to volume (**Figure 9A**, right panel). We observed a similar phenomenon in GluA3^{KO} (**Figure 9B**), although the synapses resided in a smaller range along the Z-axis. GluA2 and GluA4 intensities per synapse were positively related in both genotypes (**Figure 9C**, left). GluA2 and GluA4 intensities were positively related with CtBP2 intensities, but the relationships were less apparent in GluA3^{KO} (**Figure 9C**, center and right), consistent with the increase in CV measured for GluA2 and GluA4 intensities per synapse in GluA3^{KO} relative to GluA3^{WT} (**Figure 7**). Plotting the GluA4:GluA2 intensity ratio as a function of Z-position revealed that increases of the GluA4:GluA2 intensity ratios in GluA3^{KO} relative to GluA3^{WT} tended to be greater for synapses on the pillar side than the modiolar side (**Figure 9D**). In summary, synapse alterations in GluA3^{KO} were greatest on the pillar side, suggesting defective molecular differentiation of synapse properties along the morphological modiolar-pillar axis.

Discussion

Hearing depends on the activation of AMPARs on the post-synaptic terminals of auditory nerve fibers (Ruel et al., 1999; Glowatzki and Fuchs, 2002). Cochlear AMPARs are tetrameric heteromers comprised of the pore-forming subunits GluA2, 3, and 4, where the absence of GluA2 results in a CP-AMPA channel with increased permeability to Ca^{2+} and Na^+ . AMPAR tetramers assemble as dimers of dimers, with the GluA2/3 dimer being energetically favored and prominent in the brain (Greger et al., 2019). Our study shows that postsynaptic GluA3 subunits are required for the appropriate assembly of AMPAR GluA2 and GluA4 subunits on mammalian cochlear afferent synapses. Remarkably, we find that GluA3 is also essential for presynaptic ribbon modiolar-pillar morphological distinctions. We propose that postsynaptic GluA3 subunits at IHC-ribbon synapses may perform an organizational function beyond their traditional role as ionotropic glutamate receptors.

In the absence of GluA3 subunits, we observed a reduction in GluA2 subunits and an increase in GluA4 subunits at the ribbon synapses of 5-week-old male mice (**Figures 6-9**), preceding the decline of cochlear output observed at 8 weeks (García-Hernández et al., 2017). Taken together with previous work, we hypothesize that the 5-week-old GluA3^{KO} cochlea of male mice is in a pathological but pre-symptomatic, vulnerable state. In GluA3^{WT} mice on C57BL/6 background, synapse components (ribbons, PSDs, SVs) tended to be larger on the modiolar side in electron microscopy (**Figures 3-5**). Without GluA3 the pillar-side synaptic components were enlarged in GluA3^{KO} relative to GluA3^{WT}, including a ~ 50% increase in mean PSD surface area (**Figure 5A**), but the immunofluorescent volumes of synaptic AMPARs were concomitantly reduced on the pillar side in GluA3^{KO} relative to the modiolar side and relative to GluA3^{WT} (**Figure 8A**). This mismatch between changes in PSD size and changes in AMPAR cluster-size suggest misregulation of AMPAR density in the PSD in the absence of GluA3. In mice, SGN fibers

contact IHCs in the differentiating organ of Corti already at birth. Synaptic ribbons and synaptic membrane densities mature over the following 3-4 weeks (Sobkowicz et al., 1986; Wong et al., 2014; Michanski et al., 2019; Payne et al., 2021). Future studies should determine if these changes in synapse ultrastructure and molecular composition result from disruption of embryonic or early postnatal development and/or later postnatal maturation.

GluA3 is required for appropriate AMPAR assembly at IHC-ribbon synapses.

Noise-induced cochlear synaptopathy is caused by excitotoxic over-activation of AMPARs due to excessive glutamate release from the sensory inner hair cells (Puel et al., 1998; Kim et al., 2019). Antagonizing the Ca^{2+} -permeable subset of AMPARs (CP-AMPA) pharmacologically can prevent noise-induced synaptopathy while allowing hearing function to continue through activation of Ca^{2+} -impermeable AMPARs (Hu et al., 2020). In the absence of GluA3, GluA2/4 would be the only heterodimer. Homodimers can form and homomeric tetramers may exist, but non-GluA2 subunits preferentially heterodimerize with GluA2 subunits because homodimers are less stable energetically (Rossmann et al., 2011; Zhao et al., 2017), suggesting that GluA2/4 heterodimers should be predominant in GluA3^{KO}. However, we find that loss of GluA3 alters GluA2 and GluA4 subunit relative abundance, increasing the GluA4:GluA2 ratio (**Figures 8D, 9D**), which may increase the number of GluA2-lacking CP-AMPA at cochlear ribbon synapses of the GluA3^{KO} mice by forcing GluA4 homodimerization. The increase in CP-AMPA in the GluA3^{KO} could make the IHC-ribbon synapses more vulnerable to excitotoxic noise trauma as the cochlea matures and ages. In support of this, male GluA3^{KO} mice have reduced ABR wave-1 amplitude relative to GluA3^{WT} mice by 2-months of age and elevated ABR thresholds by 3-months of age (Garcia-Hernandez et al., 2017). Although young male GluA3^{KO} mice have ABR and synapse numbers similar to WT (**Figures 1, 6**), we hypothesize these molecular-anatomical alterations to AMPAR subunits result in synapses with increased

vulnerability to AMPAR-mediated excitotoxicity that lead to synapse loss and hearing loss as the mice age in ambient sound conditions.

It is important for future studies to determine the effects on cochlear ribbon synapses when GluA3 is removed after cochlear maturation, in comparison with the present study in which GluA3 is absent congenitally resulting in direct and indirect effects. How are the amplitude and kinetics of synaptic transmission altered under these conditions? If two synapses have the same number of AMPARs, the synapse with a greater proportion of CP-AMPARs would have increased postsynaptic current amplitude. However, the increase in GluA4 seems to be outweighed by the reduction in GluA2 and the absence of GluA3 when measuring total AMPAR volume or fluorescence per synapse, suggesting fewer AMPARs per synapse in GluA3^{KO} (**Figure 8**). In the context of homeostatic synaptic plasticity (Turrigiano, 2012), an increase in synaptic current size due to increased proportion of CP-AMPARs could be compensated by net removal of AMPARs. Thus, future studies will need to determine if these synapses suffer from postsynaptic currents that are too large, too small, or similar in size with altered single-channel conductance.

Most knowledge of AMPAR subunit composition comes from studies on neurons in the brain, where GluA1 subunits are highly expressed. For example, AMPARs of hippocampal CA1 neuronal synapses are predominantly comprised of GluA1/2 heteromers (~ 80%; Lu et al., 2009). Cochlear AMPARs are unique because mature SGNs do not express GluA1 (Niedzielski and Wenthold, 1995; Matsubara et al., 1996; Parks, 2000; Shrestha et al., 2018; this study). In the ascending auditory pathway, the presynaptic terminals of SGNs release glutamate onto neurons in the brainstem's cochlear nucleus where, as in the cochlea, AMPARs appear to lack GluA1 (**Figure 1B, right**). In the cochlea and cochlear nucleus, elimination of GluA3 did not result in GluA1 expression (**Figure 1B, left and right**). Given the influences of GluA1 subunits

in AMPAR activity-dependent plasticity in the brain (Lee et al., 2010), and considering their absence in the mature cochlea, the rules governing AMPAR dynamics in the inner ear are largely unknown and likely to be unique.

The duration of the postsynaptic current and thus the net influx of charge is largely determined by AMPAR desensitization, which is regulated by the proportion of *flip* and *flop* splice variants of GluA subunits (Sommer et al., 1990; Monyer et al., 1991; Mosbacher et al., 1994; Koike et al., 2000). *Flip* subunits desensitize more slowly than *flop* subunits, resulting in slower decays of AMPAR-mediated currents (Trussell and Fischbach, 1989; Lawrence and Trussell, 2000; Gardner et al., 2001; Quirk et al., 2004; Pei et al., 2007). Changes in transcription and mRNA splicing of AMPAR subunits may influence excitotoxicity. For example, a decrease in GluA2 and GluA3 *flop* isoforms leads to elevated intracellular Ca^{2+} levels and increased death of retina ganglion cells after glucose deprivation (Park et al., 2016). At synapses between auditory nerve fibers (endbulbs) and bushy cells in the cochlear nucleus, the lack of GluA3 results in a lower proportion of *flop* subunits (Antunes et al., 2020). In contrast, we find the absence of GluA3 did not significantly alter transcription and mRNA splicing of GluA2 and GluA4 isoforms in the cochleae of 5-week-old GluA3^{KO} mice, arguing against the possibility that such alterations underlie the pathology of IHC-ribbon synapses in GluA3^{KO} mice (**Figure 1**). We note that our method of isoform analysis was from whole temporal bones, including outer hair cell synapses and vestibular hair cell synapses. Contamination from outer hair cell synapses is likely to be small due to low AMPAR expression levels (Weisz et al., 2012; Martinez-Monedero et al., 2016). However, the presence of the vestibular synapses and/or the mixing of synapses from the whole cochlea may have prevented us from detecting changes in isoform expression at the level of individual synapses. Overall, in the inner ear in the absence of GluA3, *flop* isoforms of GluA2 and GluA4 were more abundant than *flip* isoforms, as in WT. Future patch-clamp studies are required to test AMPAR desensitization in the absence of GluA3 at the cellular level.

Potential trans-synaptic role of GluA3 at IHC-ribbon synapses.

Pre- and post-synaptic ultrastructural features of IHC-ribbon synapses are disrupted in the organ of Corti of GluA3^{KO} mice (**Figures 3-5**). This is reminiscent of the ultrastructure of endbulb synapses in the cochlear nucleus of GluA3^{KO} mice, which is altered due to trans-synaptic developmental effects, where the absence of GluA3 increases synaptic depression by increasing the initial probability of vesicle release, slowing vesicle replenishment, and reducing the readily releasable pool of synaptic vesicles through unknown mechanisms (García-Hernández et al., 2017; Antunes et al., 2020). In the cochlea, modiolar-pillar ultrastructural differences among ribbon synapses were eliminated or reversed in GluA3^{KO}. Our ultrastructural analysis shows the absence of GluA3 resulted in the loss of the modiolar-pillar difference in PSD surface area seen in GluA3^{WT}, due to larger PSDs on the pillar side of GluA3^{KO} relative to GluA3^{WT}. At endbulb synapses, an increase in PSD surface area or thickness, and changes in SVs size have been observed in congenitally deaf cats and mice (Lee et al., 2003; Ryugo et al., 1997, 2005), and after conductive hearing loss (Clarkson et al., 2016). Similarly, the increase in PSD surface area and larger SVs of pillar-side synapses may represent initial pathological structural signs in the absence of GluA3.

Through development, the ribbon-shape changes from largely round to oval, droplet-like, or wedge-like shapes (Wong et al., 2014; Michanski et al., 2019). Absence of GluA3 during development resulted in ribbons with shorter long-axes that were more spherical relative to GluA3^{WT}. This finding is consistent with a developmental defect in a process of ribbon maturation, whereby modiolar-side ribbons become longer and less spherical between 2.5-weeks and 5-weeks of age in C57BL/6 WT mice (Payne et al., 2021). While GluA3^{KO} ribbons were shorter in long-axis and more rounded in TEM than those from GluA3^{WT}, they also tended to have larger volumes particularly on the pillar side, suggesting lengthening of the short ribbon

axis in GluA3^{KO}. Finally, loss of GluA3 eliminated the modiolar-pillar difference in SV size observed in WT, due to an increase in SV size on the pillar side of GluA3^{KO}. We note that other studies of IHC ribbon synapses have identified increased SV size as a phenotype in endophilin KO and in AP180 KO mice (Kroll et al., 2019; 2020), although modiolar and pillar comparisons were not made.

Our ultrastructural data suggest that postsynaptic GluA3 subunits at IHC-ribbon synapses may perform an organizational function beyond their traditional role as ionotropic glutamate receptors. The mechanisms are still unclear, but evidence shows that AMPARs convey a retrograde trans-synaptic signal essential for presynaptic maturation (Tracy et al., 2011). AMPAR subunits in the cochlea may interact with the trans-synaptic adhesion factors Neuroligins and Neurexins (Heine et al., 2008; Hickox et al., 2017; Ramirez et al., 2022). GluA3 is required for the functional development of the presynaptic terminal and the structural maturation of SV size in endbulb auditory nerve synapses in the cochlear nucleus (Antunes et al., 2020). Altered SV size together with a change in the number of AMPARs and their clustering at the synapse contribute to quantal size variation and altered synaptic transmission (Levy et al., 2015). The number of AMPARs at IHC-ribbon synapses is undetermined but with a synaptic surface area ranging 0.1 – 1.5 μm^2 (Liberman, 1980; Payne et al., 2021) or 0.3 – 0.8 μm^2 (current study), it is estimated several hundred to a few thousand AMPARs at each PSD (Momiya et al., 2003). In GluA3^{KO} mice, we find that despite the decrease in GluA2 and the larger increase of GluA4, the overall intensity and volume of the AMPAR subunit immunolabeling at IHC-ribbon synapses decreases when compared to WT synapses, primarily due to loss of GluA3. An increase in relative abundance of CP-AMPA and a decreased overall abundance of AMPARs in GluA3^{KO} are expected to have opposing effects on the size of the synaptic current evoked by glutamate. The ABR wave-1 amplitude is unaltered in male GluA3^{KO} at 5-weeks of age suggesting a similar hearing sensitivity to WT mice. However, ABR

peak amplitudes are reduced in the male KO at 8 weeks of age (García-Hernández et al., 2017). To strengthen and confirm the potential trans-synaptic role of GluA3 at IHC-ribbon synapses and to compare synaptic strength, further electrophysiological studies need to determine the existence of altered quantal size and quantal content in the GluA3^{KO}.

In the cochlea, afferent synaptic contact formation on the IHC, characterized by a demarcated pre- and postsynaptic density, often precedes ribbon attachment at the presynaptic active zone (AZ) membrane. Ribbon attachment occurs around embryonic day 18 (E18) (Michanski et al., 2019). The presence of postsynaptic AMPARs in those embryonic IHC-ribbon synapses has not been reported. However, patches of GluA2/3 AMPAR subunit immunolabeling were observed during the first postnatal week, juxtaposed to the presynaptic ribbon marker RIBEYE (Wong et al., 2014). Fusion of ribbon precursors extends after hearing onset and is a critical step in presynaptic AZ formation and maturation (Michanski et al., 2019). This maturation of synaptic ribbons may be essential for the functional maturation of afferent synaptic transmission within the cochlea. In mice lacking synaptic ribbons features like PSDs, presynaptic densities, voltage-gated Ca²⁺ channels, and bassoon seem to develop relatively independently of ribbon presence, but spike patterns in the auditory nerve fibers are altered (Jean et al., 2018; Becker et al., 2018). It is possible that GluA3 plays a direct or indirect role in the recruitment and maintenance of pre- and post-synaptic proteins for example, via its *N*- and *C*-terminus domains. Postsynaptic PDZ domain AMPAR *C*-terminus interacting proteins such as PSD95 are present at IHC-ribbon synapses early during postnatal development (Tong et al., 2013; Wong et al., 2014). PSD95 interacts with the cell adhesion proteins Neuroligins (Irie et al., 1997; Jeong et al., 2019). Neuroligin-3 and to a lesser extent Neuroligin-1 are essential to cochlear function (Ramirez et al., 2022). In the CNS, alignment of postsynaptic AMPARs, PSD95, and Neuroligin-1 together with the pre-synaptic protein RIM form nanocolumns (Tang et al., 2016) thought to represent essential elements of trans-synaptic connections. The existence of such nanocolumns at ribbon

synapses, where several release sites may reside around each ribbon, is unknown, but the same proteins are present (Jung et al., 2015; Krinner et al., 2017; Picher et al., 2017; Hickox et al., 2017; Ramirez et al., 2022). To understand further the synaptic mechanisms of hearing and hearing loss, it will be essential to identify the full complement of cleft-spanning adhesion proteins that interact with AMPARs at IHC synapses, in particular with GluA3.

Materials and Methods

Animals

A total of 26 C57BL/6 wild type (GluA3^{WT}, n= 13) and GluA3-knockout (GluA3^{KO}, n= 13) mice were used in this study. The *Gria3* gene encodes the GluA3 protein, one of four AMPAR pore-forming subunits (GluA1-4) encoded by four genes *Gria1-4*. Generation of the GluA3^{KO} mice has been previously described (García-Hernández et al., 2017; Rubio et al., 2017). Male WT and KO mice from two separate colonies were compared at five weeks of age following normal rearing in an animal facility with 55-75 dB SPL ambient sound pressure level over time (unweighted mean SPL, 2 kHz – 80 kHz, Sensory Sentinel, Turner Scientific). Mice were fed *ad libitum* and maintained on a 12-hour light/12-hour dark daily photoperiod. All experimental procedures were in accordance with the National Institute of Health guidelines and approved by the University of Pittsburgh Institutional Animal Care and Use Committee.

Auditory Brainstem Recordings (ABR)

To test the auditory output of the GluA3^{WT} and GluA3^{KO} mice, we performed ABR as previously described (Clarkson et al., 2016; García-Hernández et al., 2017, 2022; Weisz et al., 2021). Recordings were conducted under isoflurane anesthesia in a soundproof chamber and using a Tucker-Davis Technologies (Alachua, FL) recording system. Click or tone stimuli were presented through a calibrated multi-field magnetic speaker connected to a 2-mm diameter

plastic tube inserted into the ear canal. ABR were recorded by placing subdermal needle electrodes at the scalp's vertex, at the right pinna's ventral border, and the ventral edge of the left pinna. ABR were recorded in response to broadband noise clicks (0.1 ms) or tone pips of 4, 8, 12, 16, 24, and 32 kHz (5 ms). Stimuli were presented with alternating polarity at a rate of 21 Hz, with an inter-stimulus interval of 47.6 ms. The intensity levels used were from 80 dB to 10 dB, in decreasing steps of 5 dB. The waveforms of 512 presentations were averaged, amplified 20x, and digitalized through a low impedance preamplifier. The digitalized signals were transferred via optical port to an RZ6 processor, where the signals were band-pass filtered (0.3 – 3 kHz) and converted to analog form. The analog signals were digitized at a sample rate of ~200 kHz and stored for offline analyses. Hearing threshold levels were determined from the averaged waveforms by identifying the lowest intensity level at which clear, reproducible peaks were visible. Wave 1 amplitudes were compared between GluA3^{WT} and GluA3^{KO} mice. For measurements of amplitudes, the peaks and troughs from the click-evoked ABR waveforms were selected manually in BioSigRZ software and exported as CSV files. The peak amplitude was calculated as the height from the maximum positive peak to the next negative trough.

Immunohistochemistry and immunofluorescence

A total of 14 mice (GluA3^{WT} n= 7; GluA3^{KO} n=7) were anesthetized with a mixture of ketamine (60 mg/kg) and xylazine (6.5 mg/kg) and were transcardially perfused with 4% paraformaldehyde (PFA) in 0.1M phosphate buffer (PB) pH= 7.2. After 10 minutes of transcardial perfusion, cochleae and brains were removed from the skull and postfixed for 45 minutes on ice. At the beginning of postfixation the stapes was removed, a hole was opened at the apex of the cochlea bone shell, and each cochlea was perfused with the same fixative through the oval window. After postfixation, the cochleae and brains were washed in 0.1M phosphate buffered saline (PBS).

Four cochleae (2 of each genotype) were decalcified in 10% EDTA in PBS for 24 hours, cryoprotected in 10%, 20%, and 30% sucrose in 0.1M PBS, frozen on dry ice with tissue freezing medium (Electron Microscopy Sciences, Hatfield, PA), and stored at -20°C for up to one month. Brains were cryoprotected in the same sucrose dilution gradient and frozen on dry ice. Cochleae were sectioned at 20 µm thickness with a cryostat and were mounted on glass slides. Brains were cut with a slicing vibratome at 50-60 µm thickness and collected on culture wheel plates containing 0.1M PBS. Cochlea and brain sections followed standard immunofluorescence and immunohistochemistry protocols described in Douyard et al. (2007) and Wang et al. (2011). Primary rabbit polyclonal antibodies against GluA2 (Millipore, AB1768; RRID:AB_2247874), GluA4 (Millipore, AB1508; RRID:AB_90711), and GluA1 (a gift from Robert J. Wenthold; Douyard et al., 2007) were used at a 1:500 dilution in 0.1M PBS. Cochlear sections were incubated with an Alexa-594 goat-anti-rabbit secondary antibody (1:1000; Life Tech.). Brain slices were incubated in a biotinylated secondary antibody goat anti-rabbit (1:1000; Jackson Laboratories) in 0.1M PBS. Then, brain sections were incubated in avidin-biotin-peroxidase complex (ABC Elite; Vector Laboratories; 60 min; RT), washed in 0.1M PBS, and developed with 3, 3-diaminobenzidine plus nickel (DAB; Vector Laboratories Kit; 2-5 min reaction). Sections were analyzed with an Olympus BX51 upright microscope, and digital images were captured with the CellSens software (Olympus S.L.).

The other ten cochleae (5 of each genotype) were shipped overnight to Washington University in Saint Louis in 0.1M PBS containing 5% glycerol for wholemount immunolabeling and confocal analysis of presynaptic ribbons (CtBP2/Ribeye) and postsynaptic AMPAR subunits GluA2, GluA3, and GluA4 as previously described (Jing et al., 2013; Ohn et al., 2016; Sebe et al., 2017; Kim et al., 2019; Hu et al., 2020). Primary antibodies: CtBP2 mouse IgG1 (BD Biosciences 612044; RRID:AB_399431), GluA2 mouse IgG2a (Millipore MAB397; RRID:AB_2113875),

GluA3 goat (Santa Cruz Biotechnology SC7612), and GluA4 rabbit (Millipore AB1508; RRID:AB_90711) were used with species-appropriate secondary antibodies conjugated to Alexa Fluor (Life Tech.) fluorophores excited by 488, 555, or 647 nm light in triple-labeled samples mounted in Mowiol. Samples were batch processed using the same reagent solutions in two cohorts, each including WT and KO mice. Although southern blot, western blot, and freeze-fracture post-embedding immunogold-labeling confirmed a lack of *Gria3* DNA or GluA3 protein subunit expression in GluA3^{KO} mice (García-Hernández et al., 2017; Rubio et al., 2017; in those two studies an antibody against the N-terminus domain of GluA3 was used), we found that the polyclonal GluA3 C-terminal antibody (SC7612) showed weak binding to cochlear synapses in GluA3^{KO} tissue. This false “anti-GluA3” signal on synapses in the KO presumably results from binding of the GluA3 antibody to the GluA2 C-terminus, as stated in the Santa Cruz specification sheet (<https://datasheets.scbt.com/sc-7612.pdf>), due to sequence similarity between GluA2 and GluA3 (Dong et al., 1997). Although this artifact in GluA3^{KO} is not visible when the brightness levels are set to avoid saturation in the corresponding GluA3^{WT} images, we measured the false signal in GluA3^{KO} and estimated it to be ~ 10% of the signal in GluA3^{WT} (not shown). Thus, approximately 10% of the signal quantified as anti-GluA3 immunofluorescence in GluA3^{WT} may be cross-reactivity with GluA2.

Confocal Microscopy and Image Analysis

For synapse counts and measurements of intensity, volume, sphericity, and position confocal stacks were acquired with a Z-step of 0.37 μ m and pixel size of 50 nm in X and Y on a Zeiss LSM 700 with a 63X 1.4 NA oil objective lens. To avoid saturation of pixel intensity and to enable comparisons across images and genotypes, we first surveyed the samples to determine the necessary laser power and gain settings to collect all of the images. Then, using identical acquisition settings for each sample, we collected 3–4 images from each cochlea at each of the

3 cochlear regions (basal, middle, and apical, respectively) centered near tonotopic characteristic frequencies of 40, 20, and 10 kHz (Müller et al., 2005). For display only, the brightness and contrast levels were adjusted linearly in Figures 2 and 6 for visual clarity. Image analysis was performed on unadjusted, raw data.

The numbers of hair cells and paired and unpaired pre- and post-synaptic puncta were counted and manually verified after automated identification using Imaris software (Bitplane) to calculate the mean per IHC per image. The observers were blinded to mouse genotype. For each group of images from which synapses were counted or synaptic properties were measured, grand means (\pm SD) were calculated across image means (**Figures 6B, 7E and G, 8A-D**). Paired synapses were identified as juxtaposed puncta of presynaptic ribbons (CtBP2) and postsynaptic AMPARs (GluA2 and/or GluA4), which appear to partly overlap at confocal resolution (Rutherford, 2015). Unpaired (i.e., lone) ribbons were defined as CtBP2 puncta in the IHC but lacking appositional GluA2 or GluA4 puncta. For unpaired ribbons, we did not distinguish membrane-anchored from unanchored. Ribbonless synapses consisted of GluA2 and/or GluA4 puncta located around IHC basolateral membranes but lacking CtBP2. Pixels comprising puncta of synaptic fluorescence were segmented in 3D as 'surface' objects in Imaris using identical settings for each image stack, including the 'local contrast background subtraction' algorithm for automatically calculating the threshold pixel intensity for each fluorescence channel in each image. This adaptive and automatically-calculated thresholding algorithm compensated for differences in overall luminance between image stacks that would affect the volume of segmented puncta if a fixed threshold was applied across images, and avoided the potential subjective bias of setting a user-defined arbitrary threshold value separately for each image. Intensity per synaptic punctum was calculated as the summation of pixel intensities within the surface object. To associate the intensities of different GluA puncta belonging to the same synapse (**Figures 7C, 9E-H**), we generated surface objects from a virtual 4th channel equal to

the sum of the three channels (GluA2, 3, and 4; or CtBP2, GluA2, and GluA4) and then summated the pixel intensities within each of the three fluorescence channels comprising each synapse segmented as a punctum on the 4th channel. The average density of synaptic fluorescence per image (**Figure 8C**) was calculated as median punctum Intensity (a.u.) divided by median punctum Volume (μm^3) using surface objects calculated from corresponding individual fluorescence channels. To associate the volumes of different GluA puncta belonging to the same synapse (**Figure 7B**), we used the virtual 4th channel to generate masks. The mask for each synapse had a unique color value. Objects belonging to the same synapse were identified based on common overlap with the unique color value assigned to each mask. Sphericity is the ratio of the surface area of a sphere to the surface area of an object of equal volume, so sphericity of 1 means the object is a perfect sphere. To differentiate synapse position, images were used in which the row of IHCs was oriented with the modiolar-pillar dimension in the microscope's Z-axis and the organ of Corti was not sloping in the image volume, and modiolar-side and pillar-side groups were split at the midpoint of the range of synapses along the modiolar-pillar dimension.

Reverse transcription-polymerase chain reaction (RT-PCR) and quantitative PCR (qPCR)

Under isoflurane anesthesia, mice (GluA3^{WT} n= 4; GluA3^{KO} n= 4) were euthanized via cervical dislocation and decapitation. Immediately after the following decapitation, the cranium was opened, and the inner ears were removed. Inner ears were flash-frozen in liquid nitrogen and stored in -80°C for up to one month until RT-PCR. In preparation for RT-PCR, both inner ears from each individual were homogenized by hand with mortar or pestle and RNA was extracted with Trizol (Ambion by life technology). The RNA pellet (n = 3; each pellet contained the two cochleae of one mouse, except one contained the cochleae of 2 mice) was resuspended and the supernatant containing RNA from each individual's inner ears was prepared for RT-PCR using the SuperScript Strand Synthesis System kit (Invitrogen, cat. No. 11904018). The

resulting cDNA was stored at -20°C for one week or less before real-time qPCR. qPCR was performed at the Genomics Research Core at the University of Pittsburgh using EvaGreen qPCR kit (MidSci, Valley Park, MO, cat. No. BEQPCR_R) and primers for *Gria2* and *Gria4 flip* and *flop* (*Gria2* and *Gria4* encode the GluA2 and GluA4 protein, respectively), which were the same primers used successfully in a previous RT-qPCR experiment by Hagino et al. (2004). In a 25 µL PCR reaction mixture, 2 µL cDNA samples were amplified in a Chromo 4 detector (MJ Research, Waltham, MA). GAPDH or 18S rRNA were used as housekeeping genes. Each sample (consisting of RNA product of both cochleae from each mouse) was run in triplicate, and average cycle thresholds (CTs) were used for quantification. Relative abundances of each splice isoform for GluA3^{KO} males compared to GluA3^{WT} were reported as fold-change, calculated using the following equation: $2^{\Delta\Delta CT}$ ($2^{-\Delta\Delta CT}$), where $\Delta\Delta CT = (CT_{GluA3^{WT}} - CT_{GAPDH}$ or $CT_{18S\ rRNA}) - (CT_{GluA3^{KO}} - CT_{GAPDH}$ or $CT_{18S\ rRNA})$, and CT represents the cycle threshold of each cDNA sample. For a more in-depth explanation of this equation see Schmittgen and Livak (2008). Electrophoresis of 10 µL of RT-PCR products was performed using 3% agarose (SeaKem LE Agarose by Lonza) with molecular ladder gel containing 0.5 µg/mL ethidium bromide in 0.5x tris-acetate-ethylenediaminetetraacetic acid (TAE) buffer (pH: 8.0) and run at 100 V for 60 min. The size and thickness of the agarose gel, reagents, and other conditions were kept constant. The band-size and DNA concentration of each PCR amplicon was determined by comparison to the corresponding band in the molecular weight ladder (Gene Ruler 100 BP DNA ladder Thermo Scientific). The amplicon images (RT-PCR bands) in the gel were captured under ultraviolet (UV) light and documented using a Bio Rad Molecular Imager Gel Doc RX+ Imaging system. All the parameters and experimental conditions used were kept constant throughout the study. The image was saved (in JPEG format) on a computer for digital image analysis using ImageJ software. The mean gray value (MGV) of each band was determined with NIH-ImageJ software (<https://imagej.nih.gov/ij/>). Samples were normalized to GAPDH. The *flip/flop* ratio was obtained by dividing the MGVs of the *flip* by the *flop*.

794

795 Transmission Electron Microscopy (TEM)

796 Four mice (2 per genotype) were anesthetized with a mixture of ketamine (60 mg/kg) and
797 xylazine (6.5 mg/kg) and were transcardially perfused with 0.1M PB, followed by 3% PFA
798 and 1.5% glutaraldehyde in 0.1 M PB. Cochleae were dissected from the temporal bones, and
799 fixative was slowly introduced through the oval window after removing the stapes and opening a
800 hole at the apex of the cochlea bone shell. Cochleae were post-fixed overnight in the same
801 fixative at 4°C and followed a protocol slightly modified from Clarkson et al. (2016). After
802 decalcification in 10% EDTA for 24 hours at 4°C on a rotor, cochleae were washed in 0.1M
803 cacodylate buffer and postfixed with 1% osmium and 1.5% potassium ferrocyanide in
804 cacodylate buffer for 1 hour at room temperature (RT). Cochleae were dehydrated in an
805 ascending ethanol gradient (ETOH; 35%, 50% 70%, 80% 90%) and were blocked-stained with
806 3% uranyl acetate in 70% ETOH for 2 hour at 4°C before the 80% ETOH. The last dehydration
807 steps performed with 100% ETOH and propylene oxide were followed by infiltration with epoxy
808 resin (EMBed-812; Electron Microscopy Science, PA USA). Cochleae were cut with a Leica EM
809 UC7 ultramicrotome, and series of 15-20 serial ultrathin sections (70 - 80 nm in thickness) were
810 collected. Each serial ultrathin section was collected on numbered single slot gold-gilded grids
811 with formvar. Ultrathin sections were observed with a JEOL-1400 transmission electron
812 microscope (TEM; JEOL Ltd., Akishima Tokyo, Japan), and images (at x40,000 magnification)
813 of the midcochlea (~20 kHz) containing inner hair cell (IHC)-ribbon synapses of the modiolar
814 and pillar side were captured with an OriusTM SC200 CCD camera (Gatan Inc., Warrendale, PA,
815 USA). In our ultrastructural analysis, we included IHC-ribbon synapses that were clearly located
816 on either the modiolar face or the pillar face of the IHC. We did not sample every synapse in a
817 given IHC, so the proportions of modiolar-side and pillar-side synapses analyzed do not reflect
818 the relative abundance of the population. The experimenter was not blinded to mouse genotype
819 during image acquisition and analysis.

Three-Dimensional (3-D) Reconstructions and NIH Image-J Analysis of TEM micrographs

TEM micrographs (at x40,000 magnification) of the serial IHC-ribbon synapses were calibrated, aligned and reconstructed using Reconstruct software as previously described (Gómez-Nieto and Rubio, 2009; Clarkson et al., 2016, 2020; <https://synapseweb.clm.utexas.edu/software-0>; Fiala, 2005). A total of 29 (GluA3^{WT}) and 26 (GluA3^{KO}) IHC-ribbon synapses were reconstructed. In the 3D reconstructions, we used only the ultrathin sections of IHC-ribbon synapses containing the PSD. Sections containing the afferent dendrite without PSD were not included. In brief, two successive sections were aligned via rotation and translation such that corresponding structures like mitochondria in the two sections were superimposed. Linear transformation compensated for distortions introduced by the sectioning. Following alignment of the TEM sections, structures of interest were segmented visually into contours of separate objects. The thicknesses of all ultrathin sections in series were summed to account for differences in section thickness for 3D reconstructions. The subsequent linear interpolation between membrane contours in adjacent images resulted in polygonal outlines of cell membranes, PSD and synaptic ribbons. The 3-D rendering was generated as VRML files from the stacks of all contoured sections. We calculated volumes and surface areas of the structures of interest (PSDs and ribbons) by filling these contours with tetrahedra. In addition, we used the NIH Image-J software to determine the linear length of the PSD, the synaptic ribbon major axis, and synaptic vesicle (SV) size. For this analysis we used single representative TEM micrographs (at x40,000 magnification) of each serial section series, as well as representative micrographs of other IHC-ribbon synapses that were not reconstructed because the serial section series were incomplete. A total of 43 GluA3^{WT} and 53 GluA3^{KO} PSDs were used to measure the linear length; 57 GluA3^{WT} and 60 GluA3^{KO} ribbons were used to calculate the major axes and circularity. For the SVs, we drew two perpendicular lines from the edges of the external membrane, to measure the major and minor diameters. The size of each SV was calculated as (Major diameter + Minor diameter) / 2.

Four to six SVs were analyzed per synapse. In Figures 3-5, we plotted the mean SV size per synapse (GluA3^{WT} n = 45; GluA3^{KO} n = 47) and compared grand means for modiolar and pillar groups.

Statistical Analysis

Statistical analyses were performed with GraphPad Prism software (Version 9.3.1) or IGOR Pro software (Wavemetrics, Version 7.08). Complete statistical details are included in source data files online for Figures 1, 3-6, and 8. One-way or two-way ANOVA were used for comparisons of one or two independent variables, respectively. Two-tailed Mann-Whitney U Test and paired t-test were used to compare two independent groups, as indicated in the text. Paired and multiple comparisons were made using Šidák's and Tukey's tests, respectively, as indicated in source data files. Statistical significance for all tests was set to $p < \alpha$; $\alpha = 0.05$. Data are represented as mean \pm standard deviation (SD). The coefficient of variation (CV) was calculated as $CV = SD / \text{mean}$.

References

Antunes F., Rubio, ME, Kandler K. (2020) Altered synaptic transmission and plasticity in cochlear nucleus endbulb-bushy cell synapses of mice lacking the GluA3 AMPA receptor subunit. J Neurosci 40(12):2471-2484.

Azumaya CM, Davis EL, Vinson PN, Stauffer S, Sulikowski G, Weaver CD, Nakagawa T (2017) Screening for AMPA receptor auxiliary subunit specific modulators. PLoS One 12(3):e0174742.

871 Becker L, Schnee ME, Niwa M, Sun W, Maxeiner S, Talaei S, Kachar B, Rutherford MR, Ricci
872 AJ (2018) The presynaptic ribbon maintains vesicle populations at the hair cell afferent synapse,
873 eLife e30241.

874

875 Bowie D (2018) Polyamine-mediated channel block of ionotropic glutamate receptors and its
876 regulation by auxiliary proteins. *J Bio Chem* 293(48):18789-18802.

877

878 Clarkson C, Antunes FM, Rubio ME (2016) Conductive hearing loss has long-lasting structural
879 and molecular effects on pre- and post-synaptic structures of the auditory nerve in the cochlear
880 nucleus. *J Neurosci.* 36(39):10214-10227.

881

882 Clarkson C, Smeal R., Gibbons M, White JA. Rubio M.E, Wilcox KS (2020) Ultrastructural and
883 functional changes at the tripartite synapse during epileptogenesis in a model of temporal lobe
884 epilepsy. *Exp Neurol* 326:113196.

885

886 Douyard J, Shen L, Huganir RL, Rubio ME (2007) Differential neuronal and glial expression of
887 GluR1 AMPA receptor subunit, and the scaffolding proteins SAP97 and 4.1N during rat
888 cerebellar development. *J Comp Neurol* 502:141-156.

889

890 Dong H., O'Brien J., Fung E.T., Lanahan A.A., Worley P.F., Huganir R.L. (1997) GRIP: a
891 synaptic PDZ domain-containing protein that interacts with AMPA receptors. *Nature*
892 386, pages 279–284.

893

894 Fiala JC (2005) Reconstruct: a free editor for serial section microscopy. *J Microscopy* 218:52-
895 61.

896

897 García-Hernández S., Abe M., Sakimura K., and Rubio M.E. (2017) Impaired auditory
898 processing and altered synaptic structure of the endbulb synapse in mice lacking GluA3 AMPA
899 glutamate receptors *Hear Res* 344:284-294.

900

901 García-Hernández S, Rubio ME (2022) GluA4 is necessary to elicit acoustic and tactile startle
902 response. *Hear Res* 414:108410.

903

904 Gardner SM, Trussell L, Oertel D (1999) Time course and permeation of synaptic AMPA
905 receptors in cochlear nuclear neurons correlate with input. *J Neurosci* 19:8721-8729.

906

907 Gardner SM, Trussell L, Oertel D (2001) Correlation of AMPA receptor subunit composition with
908 synaptic input in the mammalian cochlear nuclei. *J Neurosci*, 21:7428-7437.

909

910 Geiger JR, Melcher T, Koh DS, Sakmann B, Seeburgh PH, Jonas P, Monyer H (1995) Relative
911 abundance of subunit mRNAs determines gating and Ca²⁺ permeability of AMPA receptors in
912 principal neurons and interneurons in rat CNS. *Neuron* 1:193-204.

913

914 Glowatzki E, Fuchs PA (2002) Transmitter release at the hair cell ribbon synapse. *Nat Neurosci*
915 5(2):147-154.

916

917 Gómez-Nieto R, Rubio ME (2009) A bushy cell network in the rat ventral cochlear nucleus. *J*
918 *Comp Neurol* 516:241-263.

919

920 Greger IH, Mayer ML. Structural biology of glutamate receptor ion channels: towards an
921 understanding of mechanism (2019) *Cur Opin Struct Biol* 57:185-95.

922

923 Hagino Y, Kariura Y, Manago Y, Amano T, Wang B, Sekiguchi M, Nishikawa K, Aoki S, Wada
 924 K, Noda M (2004) Heterogeneity and potentiation of AMPA type of glutamate receptors in rat
 925 cultured microglia. *Glia* 47(1):68-77.
 926
 927 Henley JM, Wilkinson KA (2016) Synaptic AMPA receptors composition in development,
 928 plasticity and disease. *Nat Rev Neurosci.* 2016 Jun;17(6):337-50.
 929
 930 Heine M, Thoumine O, Mondin M, Tessier B, Giannone G, Choquet D (2008) Activity
 931 independent and subunit-specific recruitment of functional AMPA receptors at
 932 neurexin/neuroligin contacts. *PNAS* 105(52):20947-20952.
 933
 934 Higuchi M, Single FN, Köhler M, Sommer B, Sprengel R, Seeburg PH (1993) RNA editing of
 935 AMPA receptor subunit GluR-B: a base-paired intron-exon structure determines position and
 936 efficiency. *Cell* 75(7):1361-1370.
 937
 938 Hickox AE, Wong AC, Pak K, Strojny C, Ramirez M, Yates JR 3rd, Ryan AF, Savas JN (2017)
 939 Global analysis of protein expression of inner ear hair cells *J Neurosci* 37(5):1320-1339.
 940
 941 Hollmann M, Hartley M, Heinemann S (1991) Ca²⁺ permeability of KA-AMPA-gated glutamate
 942 receptor channels depends on subunit composition. *Science* 252(5007):851-853.
 943
 944 Hu N, Rutherford MA, Green SH (2020) Protection of cochlear synapses from noise-induced
 945 excitotoxic trauma by blockade of Ca²⁺-permeable AMPA receptors. *PNAS* 117(7):3828-3838.

946 Irie M, Hata Y, Takeuchi M, Ichtchenko K, Toyoda A, Hirao K, Takai Y, Rosahl TW, Südhof TC
947 (1997) Binding of neuroligands to PSD-95. *Science* 277(5331):1511-1515.
948

949 Jackson AC, Milstein AD, Soto D, Farrant M, Cull-Candy SG, Nicoll RA (2011) Probing TARP
950 modulation of AMPA receptor conductance with polyamine toxins. *J Neurosci* 31(20):7511-
951 7520.
952

953 Jean P, Lopez de la Morena D, Michanski S, Tobón LMJ, Chakrabarti R, Picher MM, Neef J,
954 Jung SY, Gültas M, Maxeiner S, Neef A, Wichmann C, Strenzke N, Grabner C, Moser T (2018)
955 The synaptic ribbon is critical for sound encoding at high rates and with temporal
956 precision. *eLife* 7: e29275.

957

958 Jeong J, Pandey S, Li Y, Badger J II, Lu W, Roche KW (2019) PSD-95 binding dynamically
959 regulates NLG1 trafficking and function. *PNAS* 116(24):12035-12044.
960

961 Jing Z, Rutherford MA, Takago H, Frank T, Fejtova A, Khimich D, Moser T, Strenzke N (2013)
962 Disruption of the presynaptic cytomatrix protein Basson degrades ribbon anchorage,
963 multiquantal release, and sound encoding at the air cell afferent synapse. *J Neurosci*
964 33(10):4456-4467.
965

966 Jung S, Oshima-Takago T, Chakrabarti R, Wong AB, Jing Z, Yamanbaeva G, Picher MM,
967 Wojcik SM, Gottfert F, Predoehl F, Michel K (2015) Rab3-interacting molecules 2 α and 2 β
968 promote the abundance of voltage-gated CaV1.3 Ca²⁺ channels at hair cell active zones.
969 *PNAS* **112**: E3141–E3149.

970

971 Kim KX, Payne S, Yang-Hood A, Li SZ, Davis B, Carlquist J, V-Ghaffari B, Gantz JA, Kallogjeri
972 D, Fitzpatrick JAJ, Ohlemiller KK, Hirose K, Rutherford MA (2019) Vesicular glutamatergic
973 transmission in noise-induced loss and repair of cochlear ribbon synapses. *J Neurosci*
974 39(23):4434-4447.

975

976 Koike, M., Tsukada, S., Tsuzuki, K., Kijima, H., Ozawa, S. (2000) Regulation of kinetic
977 properties of GluR2 AMPA receptor channels by alternative splicing. *Journal of Neuroscience*,
978 20(6), pp.2166-2174.

979

980 Krinner S, Butola T, Jung S, Wichmann C, Moser T (2017) RIM-binding protein 2 promotes a
981 large number of CaV1.3 Ca²⁺-channels and contributes to fast synaptic vesicle replenishment
982 at hair cell active zones. *Front Cell Neurosci* 11:334. 10.3389/fncel.2017.00334.

983

984 Kroll, J., Jaime Tobón, L.M., Vogl, C., Neef, J., Kondratiuk, I., König, M., Strenzke, N.,
985 Wichmann, C., Milosevic, I., Moser, T. (2019) Endophilin-A regulates presynaptic Ca²⁺ influx
986 and synaptic vesicle recycling in auditory hair cells. *EMBO J* 38(5), p.e100116.

987

988 Kroll, J., Özçete, Ö.D., Jung, S., Maritzen, T., Milosevic, I., Wichmann, C., Moser, T. (2020)
989 AP180 promotes release site clearance and clathrin-dependent vesicle reformation in mouse
990 cochlear inner hair cells. *Journal of Cell Science*, 133(2), p.jcs236737.

991

992 Kumar SS, Bacci A, Kharazia V, Huguenard JR (2002) A developmental switch of AMPA
993 receptor subunits in neocortical neurons. *J Neurosci* 22(8):3005-3015.

994

995 Lawrence JJ, Trussell LO (2000) Long-term specification of AMPA receptor properties after
 996 synapse formation. *J Neurosci* 20(13):4864-4870.
 997
 998 Lee, D. J., Cahill, H. B., Ryugo, D. K. (2003) Effects of congenital deafness in the cochlear
 999 nuclei of Shaker-2 mice: an ultrastructural analysis of synapse morphology in the endbulbs of
 1000 Held. *J. Neurocytol.* 32, 229–243
 1001
 1002 Lee, H.K., Takamiya, K., He, K., Song, L., Huganir, R.L. (2010) Specific roles of AMPA receptor
 1003 subunit GluR1 (GluA1) phosphorylation sites in regulating synaptic plasticity in the CA1 region
 1004 of hippocampus. *Journal of neurophysiology*, 103(1), pp.479-489.
 1005
 1006 Levy JM, Chen X, Reese TS, Nicoll RA (2015) Synaptic consolidation normalizes AMPAR
 1007 quantal size following MAGUK loss. *Neuron* 87:534-548.
 1008
 1009 Liberman MC (1980) Morphological differences among radial afferent fibers in the cat cochlea:
 1010 an electron-microscopic study of serial sections. *Hear Res* 3(1):45-63.
 1011
 1012 Lu, W., Shi, Y., Jackson, A.C., Bjorgan, K., During, M.J., Sprengel, R., Seeburg, P.H., Nicoll,
 1013 R.A. (2009) Subunit composition of synaptic AMPA receptors revealed by a single-cell genetic
 1014 approach. *Neuron*, 62(2), pp.254-268.
 1015
 1016 Luján B, Dagostin A, von Gersdorff H (2019) Presynaptic diversity revealed by Ca²⁺-permeable
 1017 AMPA receptors at the calyx of Held synapse. *J Neurosci* 39(16):2981-2994.
 1018

1019 Martinez-Monedero, R., Liu, C., Weisz, C., Vyas, P., Fuchs, P.A. and Glowatzki, E., 2016.
 1020 GluA2-containing AMPA receptors distinguish ribbon-associated from ribbonless afferent
 1021 contacts on rat cochlear hair cells. *Eneuro*, 3(2).
 1022
 1023 Matsubara A, Laake JH, Davanger S, Usami S, Ottersen OP (1996) Organization of AMPA
 1024 receptor subunits at a glutamate synapse: a quantitative immunogold analysis of hair cell
 1025 synapses in the rat organ of Corti. *J Neurosci* 16:4457-4467.
 1026
 1027 Matsui K, Jahr CE, Rubio ME (2005) High concentration rapid transients of glutamate mediates
 1028 neuron-glia communication via ectopic release. *J Neurosci* 25:7538-7547.
 1029
 1030 Merchán-Perez A, Liberman MC (1996) Ultrastructural differences among afferent synapses on
 1031 cochlear hair cells: Correlations with spontaneous discharge rate. *JCN* 371:208-221.
 1032
 1033 Michanski S, Smaluch K, Steyer AM, Chakrabarti R, Setz C, Oestreicher D, Ficher C, Möbius
 1034 W, Moser T, Vogl C, Wichmann C (2019) Mapping developmental maturation of inner hair cell
 1035 ribbon synapses in the apical mouse cochlea. *PNAS* 116(13):6415-6424.
 1036
 1037 Momiyama A, Silver RA, Hausser M, Notomi T, Wu Y, Shigemoto R, Cull-Candy SG (2003) The
 1038 density of AMPA receptors activated by a transmitter quantum at the climbing fibre-Purkinje cell
 1039 synapse in immature rats. *J Physiol* 549(Pt 1):75-92.
 1040

1041 Monyer H, Seeburg PH, Wisden W (1991) Glutamate-operated channels: developmentally early
 1042 and mature forms arise by alternative splicing. *Neuron* 6(5):799-810.

1043

1044 Mosbacher, J., Schöpfer, R., Monyer, H., Burnashev, N., Seeburg, P.H., Ruppersberg, J.P.
 1045 (1994) A molecular determinant for submillisecond desensitization in glutamate receptors.
 1046 *Science*, 266(5187), pp.1059-1062.

1047

1048 Müller M, von Hünenbein K, Hodis S, Smolders JWT (2005) A physiological place–frequency
 1049 map of the cochlea in the CBA/J mouse. *Hear Res* 202(1-2):63-73.

1050

1051 Niedzielski AS, Wenthold RJ (1995) Expression of AMPA, kainate, and NMDA receptor subunits
 1052 in cochlear and vestibular ganglia. *J Neurosci* 15:2338-2353.

1053

1054 Ohlemiller KK, Gagnon PM (2004) Apical-to-basal gradients in age-related cochlear
 1055 degeneration and their relationship to “primary” loss of cochlear neurons. *J Comp Neurol*
 1056 479(1):103-116.

1057

1058 Ohn T-L, Rutherford MA, Jing Z, Jung S, Duque-Afonso C, Hoch G, Picher MM, Scharinger A,
 1059 Strenzke N, Moser T (2016) Hair cells use active zones with different voltage dependence of
 1060 Ca^{2+} influx to decompose sounds into complementary neural codes. *PNAS* 113(32):E4716.

1061

1062 Park YH, Broyles HV, He S, McGrady NR, Li L, Yorio T (2016) Involvement of AMPA receptor
 1063 and its flip and flop isoforms in retinal ganglion cell death following oxygen/glucose deprivation.
 1064 *Physiol Pharmacol* 57(2):508-526.

1065

1066 Parks TN (2000) The AMPA receptors of auditory neurons. *Hear Res* 147(1-2):77-91.

1067

1068 Payne SA, Jones MS, Chung H, Skigen N, Fran A, Gattani S, Vaughn K, Schwed A, Nester M,
 1069 Bhattacharyya A, Iyer G, Davis B, Carlquist J, Patel H, Fitzpatrick JAJ, Rutherford MA (2021)
 1070 Maturation of heterogeneity in afferent synapse ultrastructure in the mouse cochlea. *Front*
 1071 *Synaptic Neurosci* 13:678575.

1072

1073 Pei W, Huang Z, Niu (2007) GluR3 flip and flop: differences in channel opening kinetics.
 1074 *Biochemistry* 46:2027-2036.

1075

1076 Petitpré, C., Wu, H., Sharma, A., Tokarska, A., Fontanet, P., Wang, Y., Helmbacher, F., Yackle,
 1077 K., Silberberg, G., Hadjab, S., Lallemand, F. (2018) Neuronal heterogeneity and stereotyped
 1078 connectivity in the auditory afferent system. *Nature communications*, 9(1), pp.1-13.

1079

1080 Petitpré, C., Faure, L., Uhl, P., Fontanet, P., Filova, I., Pavlinkova, G., Adameyko, I., Hadjab, S.,
 1081 Lallemand, F. (2022). Single-cell RNA-sequencing analysis of the developing mouse inner ear
 1082 identifies molecular logic of auditory neuron diversification. *Nature communications*, 13(1), pp.1-
 1083 15.

1084

1085 Pickard L, Noël J, Henley JM, Collingridge GL, Molnar E (2000) Developmental changes in
 1086 synaptic AMPA and NMDA receptor distribution and AMPA receptor subunit composition in
 1087 living hippocampal neurons. *J Neurosci* 20(21):7922-7931.

1088

1089 Picher MM, Opri, soleanu AM, Jung S, Michel K, Schoch S, Moser T (2017). Rab interacting
1090 molecules 2 and 3 directly interact with the pore-forming CaV1.3 Ca²⁺ channel subunit and
1091 promote its membrane expression. *Front Cell Neurosci* 11:160 10.3389/fncel.2017.00160.

1092

1093 Puel JL, Ruel J, Gervais d'Aldin C, Pujol R (1998) Excitotoxicity and repair of cochlear synapses
1094 after noise-trauma induced hearing loss. *Neuroreport* 9(9):2009-2014.

1095

1096 Quirk, J.C., Siuda, E.R., Nisenbaum, E.S. (2004) Molecular determinants responsible for
1097 differences in desensitization kinetics of AMPA receptor splice variants. *Journal of*
1098 *Neuroscience*, 24(50), pp.11416-11420.

1099

1100 Raman IM, Zhang S, Trussell LO (1994) Pathway-specific variants of AMPA receptors and their
1101 contribution to neuronal signaling. *J Neurosci* 14:4998-5010.

1102

1103 Ramirez, M.A., Ninoyu, Y., Miller, C., Andrade, L.R., Edassery, S., Bomba-Warczak, E., Ortega,
1104 B., Manor, U., Rutherford, M.A., Friedman, R.A., Savas, J.N. (2022) Cochlear ribbon synapse
1105 maturation requires Nlgn1 and Nlgn3. *Iscience*, 25(8), p.104803.

1106

1107 Rossmann M, Sukumaran M, Penn AC, Veprintsev DB, Babu MM, Greger IH (2011) Subunit-
1108 selective N-terminal domain associations organize the formation of AMPA receptor heteromers.
1109 *EMBO* 30(5):959-971.

1110

1111 Rubio ME, Matsui K, Fukazawa Y, Kamasawa N, Harada H, Itakura M, Molnár E, Abe M,
1112 Sakimura K, Shigemoto R (2017) The number and distribution of AMPA receptor channels

1113 containing fast kinetic GluA3 and GluA4 subunits at auditory nerve synapses depend on the
 1114 target cells. *Brain Struct Funct* 222(8):3375-3393.

1115

1116 Ruel J, Chen, Pujol R, Bobbin RP, Puel J (1999) AMPA-glutamate preferring glutamate
 1117 receptors in cochlear physiology of adult guinea-pig. *J Physiol* 518:667-680.

1118

1119 Ruel, J., Bobbin, R.P., Vidal, D., Pujol, R., Puel, J.L. (2000) The selective AMPA receptor
 1120 antagonist GYKI 53784 blocks action potential generation and excitotoxicity in the guinea pig
 1121 cochlea. *Neuropharmacology*, 39(11), pp.1959-1973.

1122

1123 Rutherford MA (2015) Resolving the structure of the inner ear ribbon synapse with STED
 1124 microscopy. *Synapse* 69(5):242-255.

1125

1126 Rutherford MA, Moser T (2016) The ribbon synapse between type I spiral ganglion neurons and
 1127 inner hair cells. In *The primary auditory neurons of the mammalian cochlea* (pp. 117-156).
 1128 Springer, New York, NY.

1129

1130 Rutherford MA, von Gersdorff H, Goutman JD (2021) Encoding sound in the cochlea: from
 1131 receptor potential to afferent discharge. *J Physiol* 599(10):2527-2557.

1132

1133 Ryugo, D. K., Pongstaporn, T., Huchton, D. M., Niparko, J. K. (1997) Ultrastructural analysis of
 1134 primary endings in deaf white cats: morphologic alterations in endbulbs of Held. *J. Comp.*
 1135 *Neurol.* 385, 230–244.

1136

1137 Ryugo, D. K., Kretzmer, E. A., Niparko, J. K. (2005) Restoration of auditory nerve synapses in
 1138 cats by cochlear implants. *Science* 310, 1490–1492.

1139

1140 Schmid S, Guthmann A, Ruppersberg JP, Herbert H (2001) Expression of AMPA receptor
1141 subunit flip/flop splice variants in the rat auditory brainstem and inferior colliculus. J Comp
1142 Neurol 430:160-171.

1143

1144 Schmittgen TD, Livak KJ (2008) Analyzing real-time PCR data by the comparative C₉T)
1145 method. Nat Protocol 3(6):1101-1108.

1146

1147 Sebe JY, Cho S, Sheets L, Rutherford MA, von Gersdorff H, Raible DW (2017) Ca²⁺-permeable
1148 AMPARs mediate glutamatergic transmission and excitotoxic damage at the hair cell ribbon
1149 synapse. J Neurosci 37:6162-6175.

1150

1151 Shrestha, B.R., Chia, C., Wu, L., Kujawa, S.G., Liberman, M.C. and Goodrich, L.V. (2018)
1152 Sensory neuron diversity in the inner ear is shaped by activity. Cell, 174(5), pp.1229-1246.

1153

1154 Sobkowicz, H.M., Rose, J.E., Scott, G.L. and Levenick, C.V., 1986. Distribution of synaptic
1155 ribbons in the developing organ of Corti. Journal of neurocytology, 15(6), pp.693-714.

1156

1157 Sommer B, Keinänen K, Verdoorn TA, Wisden W, Burnashev N, Herb A, Köhler M, Takagi T,
 1158 Sakmann B, Seeburg PH (1990) Flip and flop: A cell-specific functional switch in glutamate-
 1159 operated channels of the CNS. *Science* 249:1580-1585.

1160

1161 Sommer B, Köhler M, Sprengel R, Seeburg PH (1991) RNA editing in brain controls a
 1162 determinant of ion flow in glutamate-gated channels. *Cell* 67(1):11-19.

1163

1164 Sun, S., Babola, T., Pregernig, G., So, K.S., Nguyen, M., Su, S.S.M., Palermo, A.T., Bergles,
 1165 D.E., Burns, J.C., Müller, U. (2018) Hair cell mechanotransduction regulates spontaneous
 1166 activity and spiral ganglion subtype specification in the auditory system. *Cell*, 174(5), pp.1247-
 1167 1263.

1168

1169 Sugden SG, Zirpel L, Dietrich CJ, Parks TN (2002) Development of specialized AMPA receptors
 1170 of auditory neurons. *J Neurobiol* 52(3):189-202.

1171

1172 Tang A-H, Chen H, Li TP, Metzbower SR, McGillavry HD, Blandpied TA (2016) A trans-synaptic
 1173 nanocolumn aligns neurotransmitter release to receptors. *Nature* 536:210-214.

1174

1175 Tong M, Brugeaud A, Edge ASB (2013) Regenerated synapses between postnatal hair cells
 1176 and auditory neurons. *JARO* 14(3):321-329.

1177

1178 Tracy TE, Yan JJ, Chen L (2011) Acute knockout of AMPA receptors reveals a trans-synaptic
 1179 signal for presynaptic maturation. *EMBO* 20:1577-1592.

1180

1181 Trussell LO (1997) Cellular mechanisms for preservation of timing in central auditory pathways.
 1182 Curr Opin Neurobiol 7:487-492.

1183

1184 Trussell, L.O., Fischbach, G.D. (1989) Glutamate receptor desensitization and its role in
 1185 synaptic transmission. Neuron, 3(2), pp.209-218.

1186

1187 Turrigiano, G., 2012. Homeostatic synaptic plasticity: local and global mechanisms for
 1188 stabilizing neuronal function. Cold Spring Harbor perspectives in biology, 4(1), p.a005736.

1189

1190 Twomey EC, Yelshanskaya MV, Vassilevski AA, Sobolevsky AI (2018) Mechanisms of channel
 1191 block in calcium-permeable AMPA receptors. Neuron 99(5):956-968.

1192

1193 Wang YX, Wenthold RJ, Petralia RS (1998) Endbulb synapses in the anteroventral cochlear
 1194 nucleus express a specific subset of AMPA-type glutamate receptor subunits. J Neurosci
 1195 18(3):1148-1160.

1196

1197 Wang Y, Manis P (2005) Synaptic transmission at the cochlear nucleus endbulb synapse during
 1198 age-related hearing loss in mice. J Neurophysiol 94(3):1814-1824.

1199

1200 Wang H, Yin G, Rogers K, Miralles C, De Blas AL, Rubio ME (2011) Monaural conductive
 1201 hearing loss alters the general expression of the GluA3 AMPA and glycine receptor $\alpha 1$ subunits
 1202 in Bushy and Fusiform cells of the cochlear nucleus. *Neuroscience*. 199:438-451

1203

1204 Weisz, C.J., Lehar, M., Hiel, H., Glowatzki, E. and Fuchs, P.A., 2012. Synaptic transfer from
1205 outer hair cells to type II afferent fibers in the rat cochlea. *Journal of Neuroscience*, 32(28),
1206 pp.9528-9536.

1207

1208 Weisz CJ, Williams S-P, G.Ferreira D, Eckard CS, Divito CB, Fantetti KN, Dettwyler SA, Cai H-
1209 M, Rubio ME, Kandler K, Seal RP (2021). Outer hair cell glutamate signaling through type II
1210 afferents activates neurons in the cochlear nucleus in response to non-damaging sounds. *J*
1211 *Neurosci* 41(13):2930–2943.

1212

1213 Wong AB, Rutherford MA, Gabrielaitis M, Pangrsic T. Göttfert F, Frank T, Michanski S, Hell S,
1214 Wolf F, Wichmann C, Moser T (2014) Developmental refinement of hair cell synapses tightens
1215 the coupling of Ca²⁺ influx exocytosis. *EMBO J* 33(3):247-267.

1216

1217 Youssoufian M, Oleskevich S, Walmsley B (2005) Development of a robust central auditory
1218 synapse in congenital deafness. *J Neurophysiol* 94(5):3168-3180.

1219

1220 Zhao H, Lomash S, Chittori S, Glasser C, Mayer ML, Schuck P (2017) Preferential assembly of
1221 heteromeric kainate and AMPA receptor amino terminal domains. *eLife* 6:e32056.

1222

Figure Legends

Figure 1. ABRs, GluA1 and GluA2 immunolabeling and qRT-PCR in GluA3^{WT} and GluA3^{KO}.

A. Mean ABR thresholds (\pm SD) were similar between male GluA3^{WT} and GluA3^{KO} mice ($F_{(1, 168)} = 2.659$, $p = 0.11$; two way-ANOVA; GluA3^{WT} $n = 13$; GluA3^{KO} $n = 13$). In GluA3^{WT} and GluA3^{KO} there was a main effect of sound intensity ($F_{(6, 168)} = 78.78$, $p < 0.0001$). For ABR wave-1 amplitudes (\pm SD), there was an effect of sound intensity ($F_{(11, 192)} = 49.62$; $p < 0.0001$), but mean amplitudes were similar between genotypes ($F_{(1, 292)} = 2.458$, $p = 0.118$; two-way-ANOVA). For ABR wave-1 latencies (\pm SD), there was a main effect of sound level in both genotypes ($F_{(1, 288)} = 47.11$, $p < 0.0001$) and mean latencies were similar between GluA3^{WT} and GluA3^{KO} mice ($F_{(1, 288)} = 0.1273$, $p = 0.7215$; two way-ANOVA).

B. Micrographs show immunolabeling for GluA1, GluA2, and GluA4 on SGN somata, and for GluA1 on the anteroventral cochlear nucleus (AVCN) and cerebellum (Crb) of GluA3^{WT} and GluA3^{KO} mice. Immunolabeling for GluA2 and GluA4 is observed on SGNs of both genotypes. In contrast, immunolabeling for GluA1 was not observed on SGNs nor in the AVCN of GluA3^{WT} or GluA3^{KO} mice, but was observed in the cerebellar Bergmann glia of both genotypes. Scale bars: 20 and 100 μ m.

C. Images of *Gria2* and *Gria4* *flip* and *flop*, and GAPDH gels of GluA3^{WT} and GluA3^{KO} inner ears. Histograms show fold change (\pm SD) of qRT-PCR product. Paired t-test, two-tailed..

Figure 2. Immunohistofluorescence of AMPAR pore-forming subunits GluA2, 3, and 4 on spiral ganglion neuron postsynaptic terminals in the organ of Corti. Confocal microscope immuno-fluorescence images of afferent ribbon synapses in organ of Corti whole-mount

samples from GluA3^{WT} (left) and GluA3^{KO} mice (right) in the mid-cochlea. Anti-GluA2 (green), -GluA3 (blue), and -GluA4 (red) label the postsynaptic AMPAR subunits encoded by the *Gria2*, *Gria3*, and *Gria4* genes, respectively. Each subpanel displays synaptic puncta of approximately 12 inner hair cells. Scale bars: 20 μ m (A, C); 10 μ m (B, D).

A. From top to bottom: GluA3^{WT} in grayscale for anti-GluA2, 3, 4, and the sum of the three. In the GluA2 subpanel, the basolateral membranes of four IHCs are indicated by dashed curves.

B. Merged color image of the region of interest indicated by the dashed rectangle in panel A. Inset on right: enlargement of the dashed rectangular region of interest on left shows 5 postsynaptic AMPA-receptor arrays of ribbon synapses from one IHC.

C. From top to bottom: GluA3^{KO} in grayscale for anti-GluA2, 3, 4, and the sum of the three.

D. Merged color image of the region of interest indicated in panel C. Inset: enlargement of a rectangular region of interest shows several postsynaptic AMPAR arrays of ribbon synapses from one IHC.

Figure 3. Ultrastructural features of GluA3^{WT} IHC-ribbon midcochlear synapses.

A-B. TEM micrographs of IHC-synapses on the modiolar (A) and pillar side (B). Aff.: afferent; IHC: inner hair cell; Eff.: efferent terminal. Scale bar: 0.5 μ m.

A'-B'. Three-D reconstructions of the IHC-ribbon synapses are shown in A and B. Representative serial electron micrograph images of modiolar-side and pillar-side ribbon synapses are shown in Figure 3-figure supplement 1.

C. Plots of the quantitative data of the surface area, and volume of the PSDs and ribbons obtained from the 3D reconstructions of GluA3^{WT} mice. The error bar corresponds to \pm SD.

D. Plots of the quantitative data from single ultrathin sections of the linear length of the PSD, major axis and circularity of the ribbons, and the average size of SVs/synapse of GluA3^{WT} mice. The error bar corresponds to \pm SD.

Figure 4. Ultrastructural features of GluA3^{KO} IHC-ribbon midcochlear synapses.

A-B. TEM micrographs of IHC-synapses on the modiolar (A) and pillar side (B) of GluA3^{KO} mice. Aff.: afferent; IHC: inner hair cell; ER.: endoplasmic reticulum/swelling. Scale bar: 0.5 μ m.

A'-B'. Three-D reconstructions of the IHC-ribbon synapses are shown in A and B. Representative serial electron micrograph images of modiolar-side and pillar-side ribbon synapses are shown in Figure 4- figure supplement 1.

C. Plots of the quantitative data of the surface area, and volume of the PSDs and ribbons obtained from the 3D reconstructions of GluA3^{KO} mice. The error bar corresponds to \pm SD.

D. Plots of the quantitative data from single ultrathin sections of the linear length of the PSD, major axis and circularity of the ribbons and the average size of SVs/synapse of GluA3^{KO} mice. The error bar corresponds to \pm SD.

Figure 5. IHC modiolar-pillar structural differences in presynaptic ribbon size, ribbon shape, and vesicle size seen in GluA3^{WT} were diminished or reversed in Gria3^{KO}.

A. Whisker plots show the quantitative data of the surface area and volume of the PSD and ribbon volume of GluA3^{WT} (black) and GluA3^{KO} (gray) mice. The error bar corresponds to \pm SD.

B. Whisker plots of the linear length of the PSD, major axis, and circularity of the ribbons of GluA3^{WT} (black) and GluA3^{KO} (gray) mice. Column histogram of the size of SVs of GluA3^{WT} (black) and GluA3^{KO} (gray). The error bar corresponds to \pm SD.

Figure 6. Inner hair cell ribbon synapse counts in 5-week-old male GluA3^{WT} and GluA3^{KO} mice.

A. Confocal microscope immuno-fluorescence images of afferent ribbon synapses in organ of Corti whole-mount samples from GluA3^{WT} (upper) and GluA3^{KO} mice (lower) in the apical, middle, and basal cochlea (left, middle, right). Anti-CtBP2 labels the Ribeye protein in presynaptic ribbons (red); Anti-GluA2 labels the postsynaptic AMPAR subunit encoded by the *Gria2* gene (green); Anti-GluA4 labels the AMPAR subunit encoded by *Gria4* (blue). Each subpanel displays synaptic puncta of approximately 4 inner hair cells. Scale bars: 10 μ m.

B. Quantification of ribbon synapse numbers in images from GluA3^{WT} (black: 2,990 synapses; n = 32 images; 5 mice) and GluA3^{KO} (gray: n = 2,814 synapses; n = 30 images; 5 mice). Each point represents the mean number of synapses per inner hair cell (IHC) per image; approximately 12 IHCs per image and 6 images per cochlea. **I)** Paired synapses per IHC were similar in number for the whole cochlea ($p = 0.94$, U: 484, $n_{WT} = 32$, $n_{KO} = 30$) and in each of 3 tonotopic regions centered at 10 kHz ($p = 0.08$, U: 59, $n_{WT} = 8$, $n_{KO} = 10$), 20 kHz ($p = 0.41$, U: 61, $n_{WT} = 10$, $n_{KO} = 10$), or 40 kHz ($p = 0.10$, U: 42, $n_{WT} = 14$, $n_{KO} = 10$). **II)** Lone or 'orphaned' ribbons (CtBP2-only) were significantly more frequent in GluA3^{KO} ($p = 0.021$, U: 44, $n_{WT} = 14$, $n_{KO} = 13$). **III)** Ribbonless synapses (GluA2+GluA4) were similar in number ($p = 0.67$, U: 100,

$n_{WT} = 14$, $n_{KO} = 13$). **IV**) Paired synapses lacking GluA4 (CtBP2+GluA2) were similar in number ($p = 0.81$, U: 39, $n_{WT} = 7$, $n_{KO} = 12$). **V**) Paired synapses lacking GluA2 (CtBP2+GluA4) were observed in GluA3^{KO} ($p = 0.028$, U: 21, $n_{WT} = 7$, $n_{KO} = 12$) but not in GluA3^{WT}.

Figure 7. Alteration of AMPAR subunit expression in GluA3^{KO} mice.

A. From images like in Figure 2: Summed pixel intensity per synapse (raw values, a.u.) for GluA2 (green), GluA4 (blue), and GluA_{Sum} (black). In each subpanel, GluA3^{WT} is on left and GluA3^{KO} is on right. Bars show mean \pm SD; $n = 3$ mid-cochlear images per genotype, assessed further in panels E-H.

B. Volume analysis of two exemplar images showing GluA4 vs. GluA2 volume per synapse (μm^3) in the mid-cochlea of GluA3^{WT} (black, $n = 148$ synapses) and GluA3^{KO} (gray, $n = 166$ synapses). The distribution of GluA4 and GluA2 puncta are shifted to smaller volumes in GluA3^{KO}, although the upper ranges are unchanged.

C. Intensity analysis of the synapses in panel B (summed pixel intensity per synapse) reveals an increase in GluA4 and decrease in GluA2 immuno-fluorescence in GluA3^{KO}. Intensity values were normalized to the maximum synapse intensity for GluA4.

D. Volume (μm^3) vs. summed pixel intensity (norm.) per synapse for GluA3^{WT} (filled circles) and GluA3^{KO} (open circles) for GluA2, 3, and 4 puncta (green, blue, red). The positive correlation is slightly sub-linear.

E. Intensity analysis (sum of pixel intensities per synapse) of postsynaptic puncta grouped from GluA3^{WT} ($n = 545$ synapses from 3 images) or GluA3^{KO} cochlea ($n = 513$ synapses from 3

images) shows reduction of overall GluA intensity ($\text{GluA}_{\text{Sum}} = \text{GluA2} + \text{GluA3} + \text{GluA4}$, gray) and reduction in GluA2 intensity (green) with increase in GluA4 intensity (red) in GluA3^{KO} . Data are normalized to the mean WT synapse intensity per group for GluA2, GluA4, or GluA_{Sum} .

F. Normalized data as in panel E displayed as cumulative distributions for GluA3^{WT} (solid line) and GluA3^{KO} (dashed lines). The overall intensity in GluA3^{KO} (black dashed line, GluA_{Sum}) is reduced relative to GluA3^{WT} (solid black line) due to lack of GluA3 and reduction in GluA2 (green) despite the relatively large increase in GluA4 (red).

G. GluA puncta volume analysis reveals a reduction of GluA2 and GluA4 volume per synapse in GluA3^{KO} relative to GluA3^{WT} . Data are normalized to the mean WT synapse volume per group for GluA2, GluA4, or GluA_{Sum} .

H. Data in panel G displayed as cumulative distributions. Instead of normalizing to the WT group mean as in panels E-G, here data was normalized to each image mean to visualize differences in the shape of the distributions between GluA3^{WT} and GluA3^{KO} .

Figure 8. Modiolar-side and Pillar-side Volume, Intensity, and Density of presynaptic ribbon and postsynaptic AMPAR subunits.

A. Quantification of CtBP2, GluA2, or GluA4 mean volume per image for GluA3^{WT} (black, $n = 2,990$ synapses from 14 images) compared to GluA3^{KO} (gray, $n = 2,814$ synapses from 14 images). Each point represents the mean number per inner hair cell (IHC) per image; approximately 12 IHCs per image. Gold bars are mean \pm SD. For CtBP2, there is an overall reduction in volume in GluA3^{KO} ($p = 0.008$, U: 144, $n_{\text{WT}} = 14$, $n_{\text{KO}} = 13$). For GluA2, the overall volume reduction in GluA3^{KO} ($p = 0.0001$, U: 168, $n_{\text{WT}} = 14$, $n_{\text{KO}} = 13$) resulted from smaller

puncta on the pillar side of GluA3^{KO} relative to GluA3^{WT} ($p = 0.0083$; U: 90, $n_{WT} = 7$, $n_{KO} = 10$) but not on the modiolar side ($p = 0.063$). For GluA4, the overall volume reduction in GluA3^{KO} ($p = 4.9e^{-6}$; U: 176, $n_{WT} = 14$, $n_{KO} = 13$) resulted from smaller puncta on the pillar side of GluA3^{KO} ($p = 0.0004$; U: 96, $n_{WT} = 7$, $n_{KO} = 10$) and on the modiolar side of GluA3^{KO} ($p = 0.0058$; U: 62, $n_{WT} = 7$, $n_{KO} = 10$) relative to GluA3^{WT}. See Figure 8-figure supplement 1.

B. Quantification of median intensities per image for data in panel A. CtBP2 intensity increased in GluA3^{KO} ($p = 0.0001$; U: 17, $n_{WT} = 14$, $n_{KO} = 13$); GluA2 intensity decreased in GluA3^{KO} ($p = 0.01$; U: 143, $n_{WT} = 14$, $n_{KO} = 13$); and GluA4 intensity decreased in GluA3^{KO} ($p = 5e^{-6}$; U: 6, $n_{WT} = 14$, $n_{KO} = 13$).

C. Increase in CtBP2 ($p = 5e^{-5}$; U: 14, $n_{WT} = 14$, $n_{KO} = 13$) and GluA4 median density per synapse ($p = 5e^{-6}$; U: 6, $n_{WT} = 14$, $n_{KO} = 13$) in GluA3^{KO} relative to GluA3^{WT}, but not GluA2 ($p = 0.63$; U: 101, $n_{WT} = 14$, $n_{KO} = 13$).

D. Increase in GluA4 : GluA2 intensity ratio in GluA3^{KO} relative to GluA3^{WT} ($p = 6e^{-7}$; U: 0, $n_{WT} = 14$, $n_{KO} = 13$).

Figure 9. Spatial trends of synapse sphericity, volume, and AMPAR subunit relative abundance in the organ of Corti.

A. Volume and sphericity per synapse vs. Z-axis-position for an exemplar GluA3^{WT} image from Figure 7 showing spatial oscillations in CtBP2, GluA2, and GluA4. **Right:** Inverse relationship between synapse sphericity and volume for CtBP2, GluA2, and GluA4.

B. For GluA3^{KO}, as in panel A.

1404

1405 **C. Left:** Normalized intensity of GluA4 vs. normalized intensity of GluA2 for GluA3^{WT} (black)
1406 and GluA3^{KO} (gray). **Center:** Normalized intensity of GluA4 vs. normalized intensity of CtBP2.
1407 **Right:** Normalized intensity of GluA2 vs. normalized intensity of CtBP2.

1408

1409 **D.** GluA4:GluA2 intensity ratio vs. Z-axis-position. Panels C-D for 6 WT and 6 KO images from
1410 the midcochlea.

1411

1412

1413 **Figure 3-figure supplement 1. Representative serial electron micrographs and**
1414 **corresponding 3D reconstructions of modiolar- or pillar-side IHC-ribbon synapses of the**
1415 **GluA3^{WT} mice.** Synapses #10 and #24 correspond to the synapses shown in Figure 3. Scale
1416 bar: 0.5 μ m

1417

1418 **Figure 4-figure supplement 1. Representative serial electron micrographs and**
1419 **corresponding 3D reconstructions of modiolar- or pillar-side IHC-ribbon synapses of the**
1420 **GluA3^{KO} mice.** Synapses #15 and #24 correspond to the synapses shown in Figure 4.
1421 Representative serial electron micrographs of one pillar-side synapse with 2 ribbons; this
1422 synapse was not included in our analysis. Scale bar: 0.5 μ m.

1423

1424 **Figure 8-figure supplement 1. Modiolar-side, pillar-side groupings and example synapses**
1425 **from GluA3^{WT} and GluA3^{KO}.** **A.** Schematic of an IHC when mounted with long axis parallel to
1426 the glass coverslip, such that the modiolar-pillar dimension of the cell is orthogonal to the cover
1427 slip. Per image, the synapses were divided into modiolar and pillar groups on either side of a
1428 dividing line defined by the midway point of the spatial extent of synapses in the modiolar-pillar

dimension (Z-axis) of the image volume. **B.** Examples of modiolar-side and pillar-side synapses in GluA3^{WT}. **C.** Examples of modiolar-side and pillar-side synapses in GluA3^{KO}.

Figure 1-source data 1. Data and statistical analysis for the ABR, PCR gels and qRT-PCR for GluA3^{WT} and GluA3^{KO} mice

Figure 1-source data 2. Raw unedited PCR acrylamide gels for *Gria2* and *Gria4 flip/flop* in GluA3^{WT} and GluA3^{KO}.

Figure 1-source data 3. Figures of the uncropped PCR acrylamide gels for *Gria2* and *Gria4 flip/flop* in GluA3^{WT}, and GluA3^{KO} with relevant bands and lanes clearly labeled.

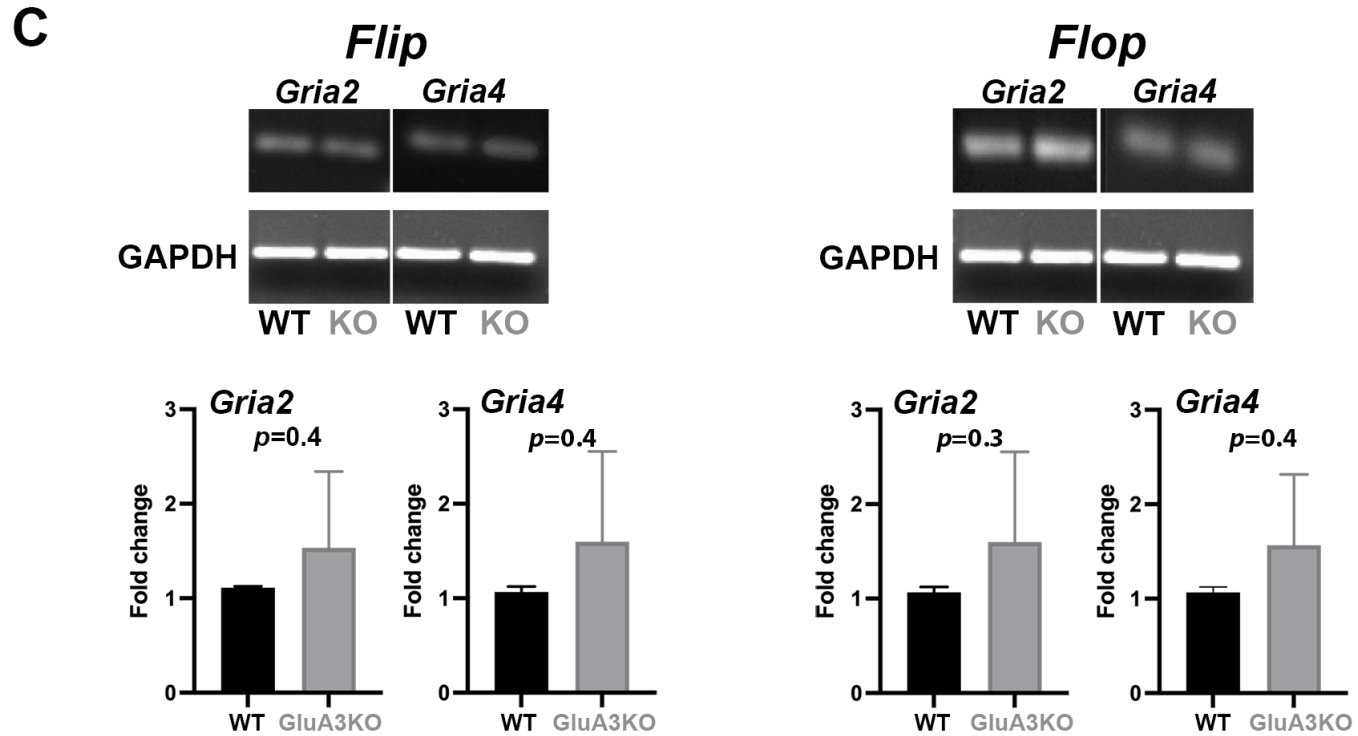
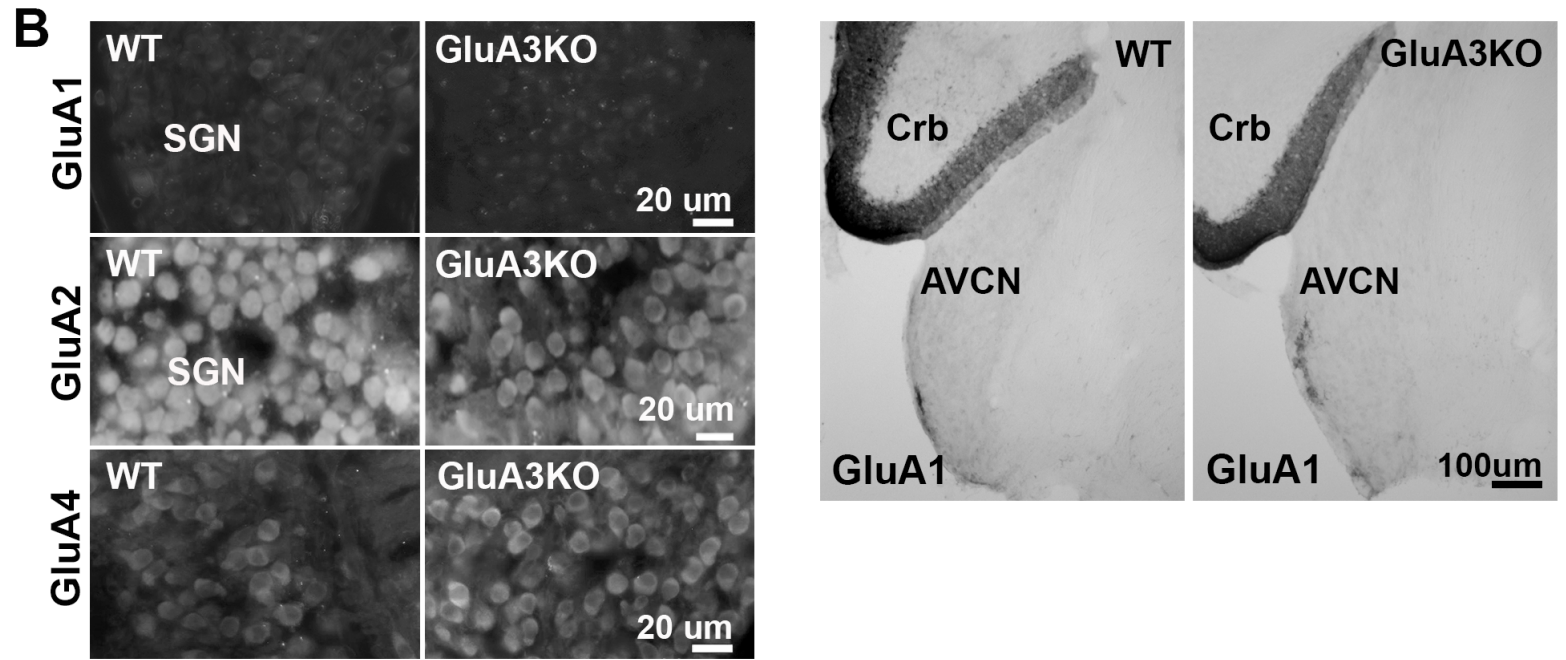
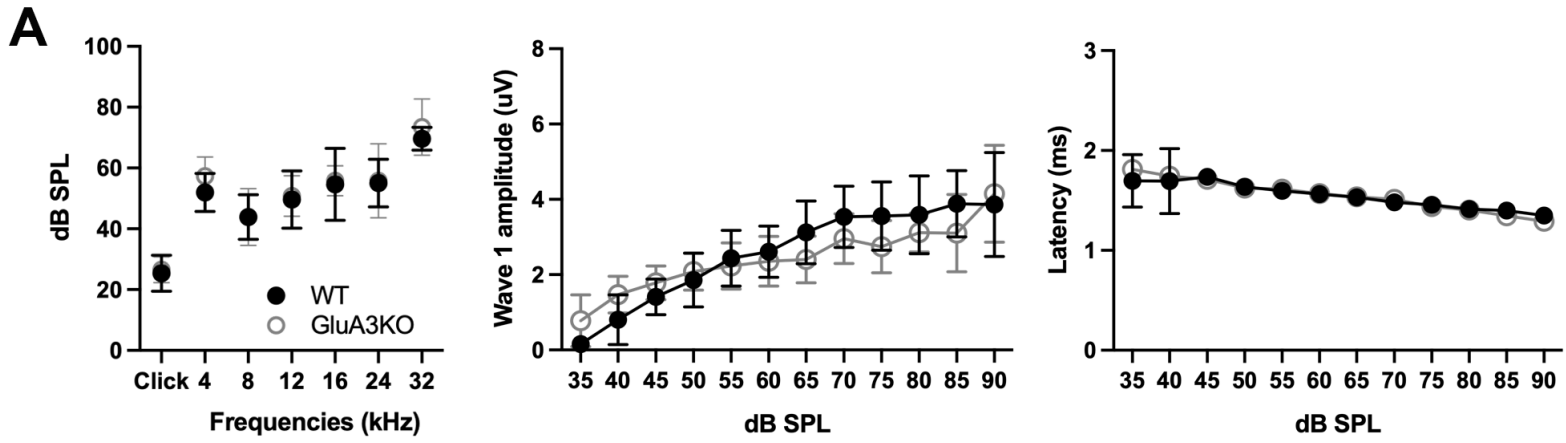
Figure 3-source data 1. Data and statistical analysis for the ultrastructural analysis of GluA3^{WT} mice.

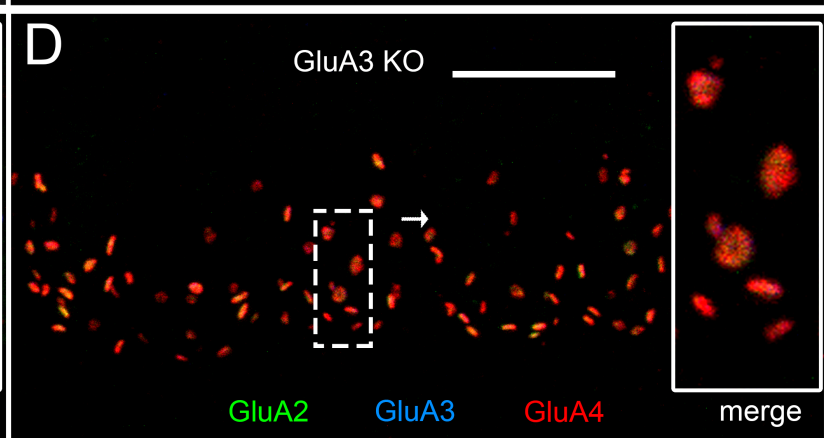
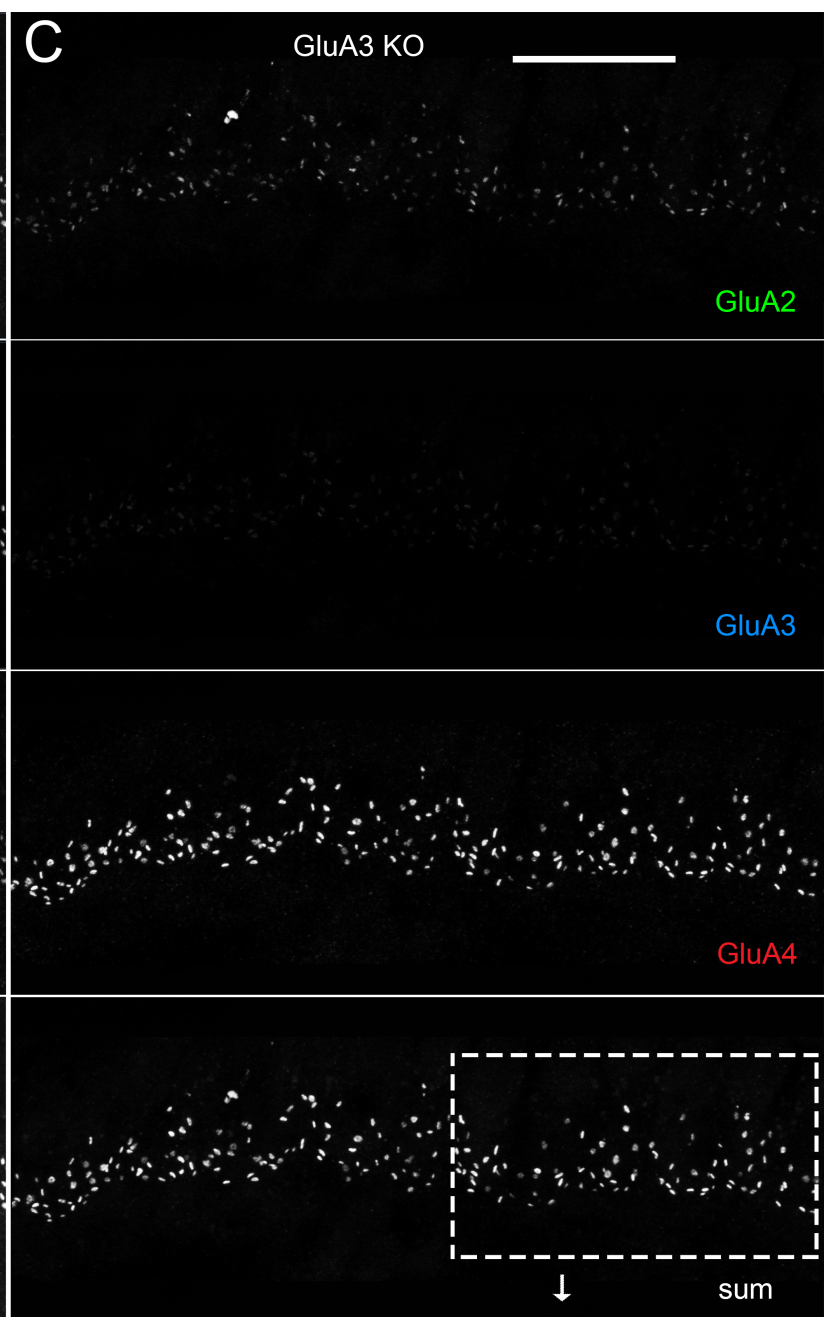
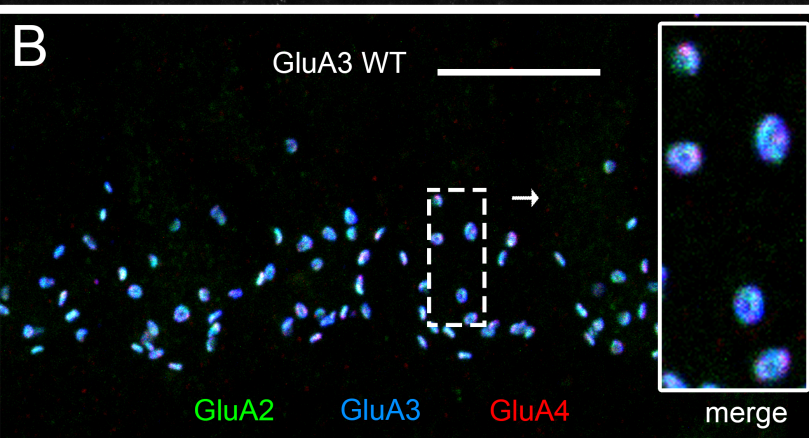
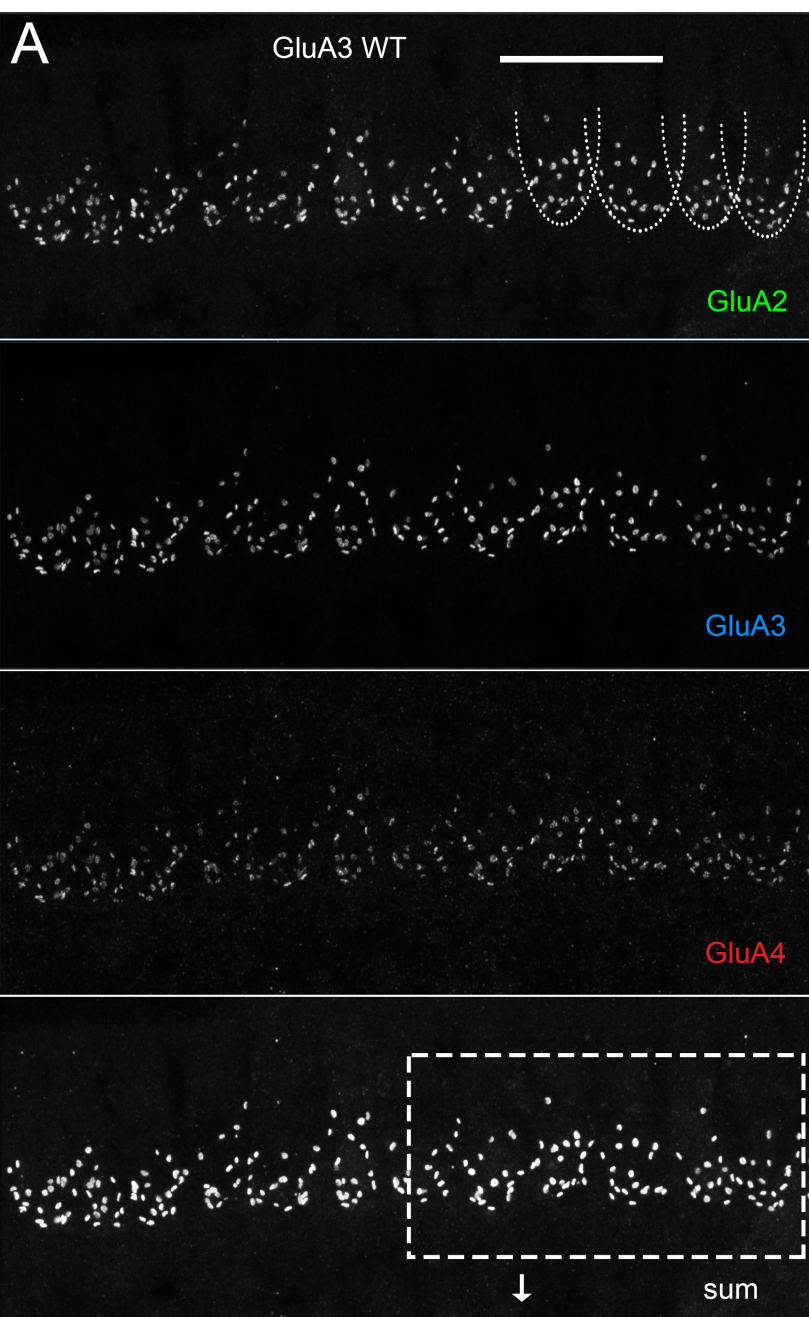
Figure 4-source data 1. Data and statistical analysis for the ultrastructural analysis of GluA3^{KO} mice

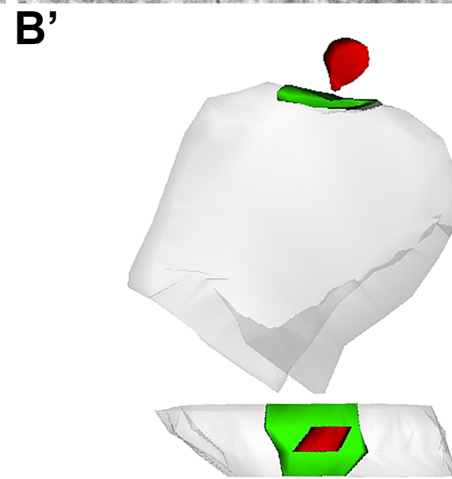
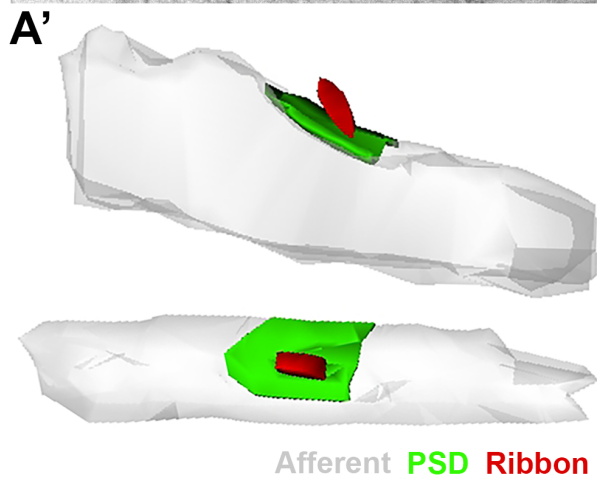
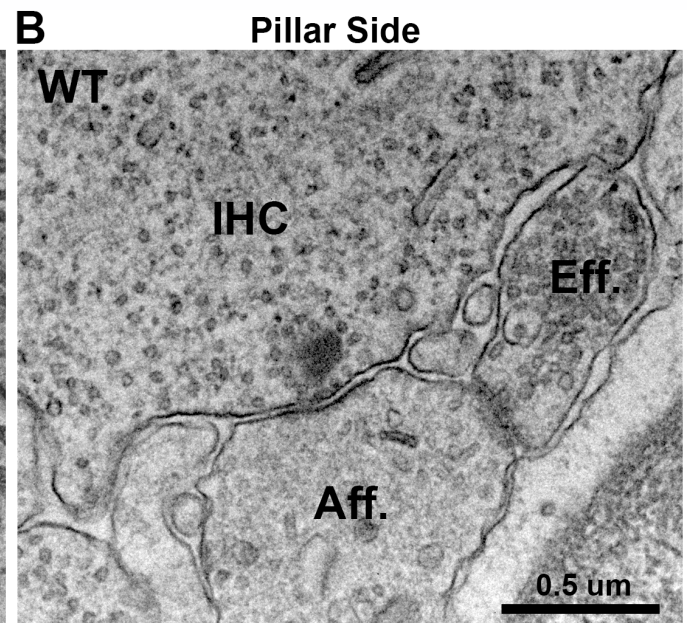
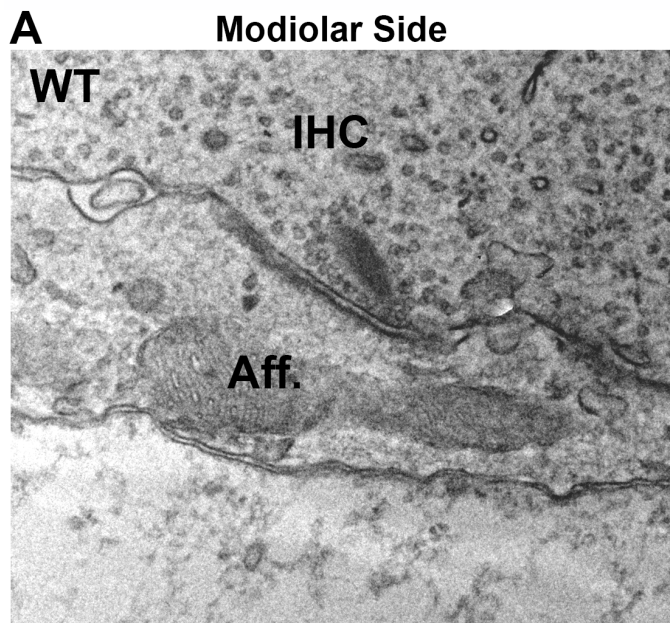
Figure 5-source data 1. Data and statistical analysis for the comparison of the ultrastructural analysis of WT vs. GluA3^{KO} mice.

Figure 6-source data 1. Confocal data and statistics of synapse counts for GluA3^{WT} and GluA3^{KO}.

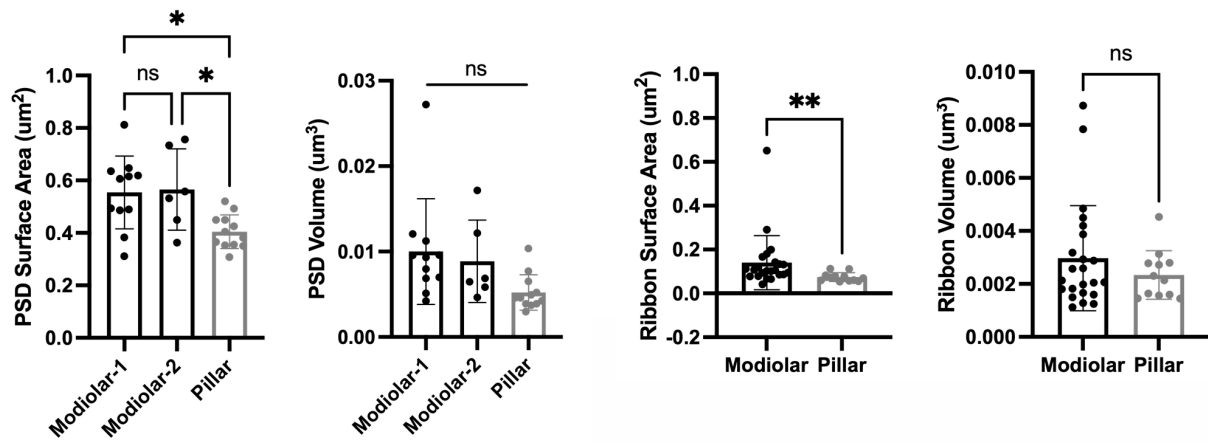
Figure 8-source data 1. Confocal data and statistics of synapse volumes and intensities for GluA3^{WT} and GluA3^{KO}.



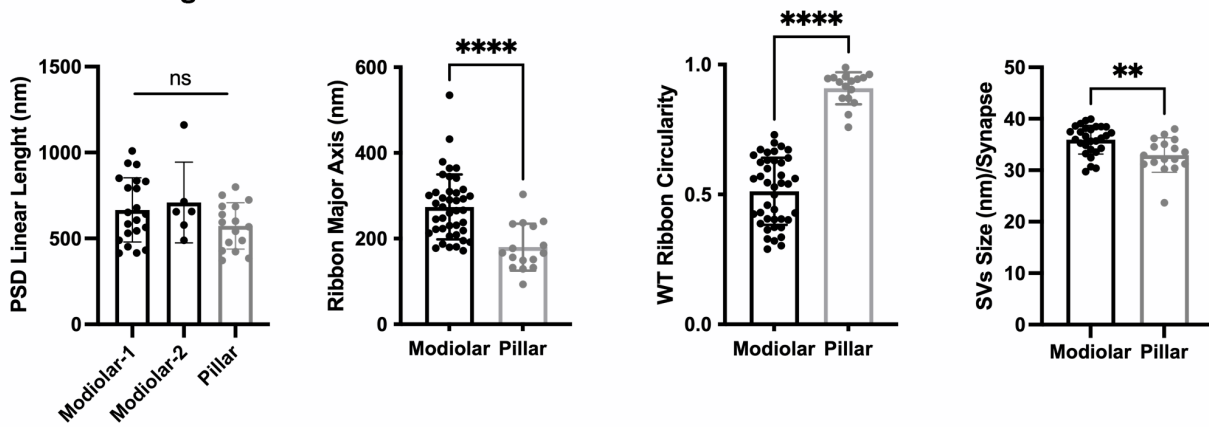


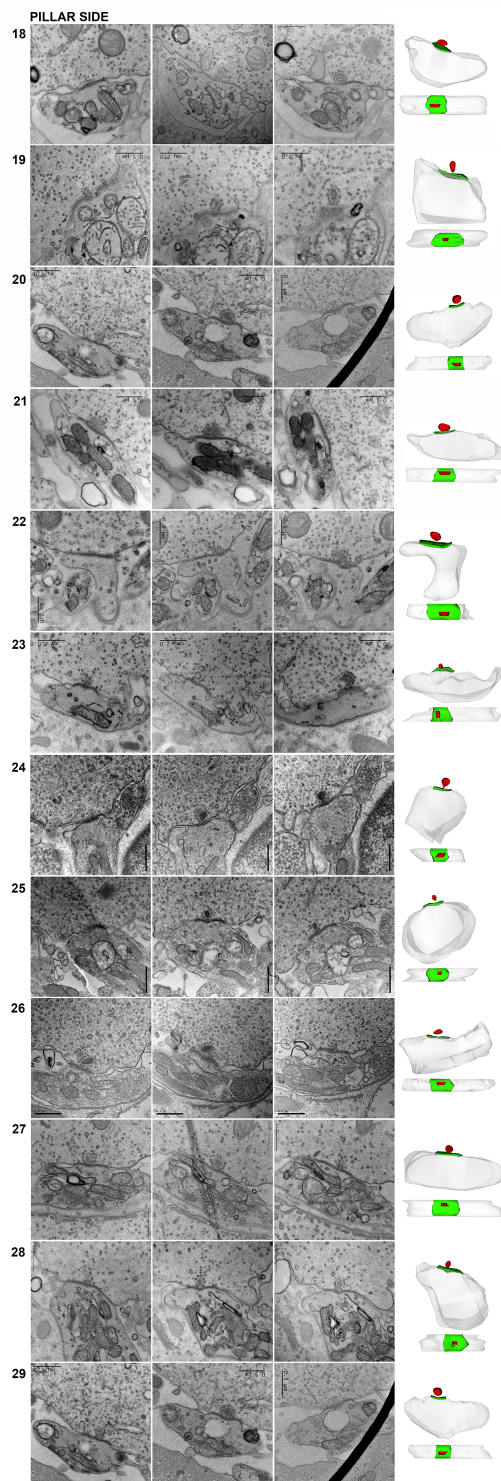
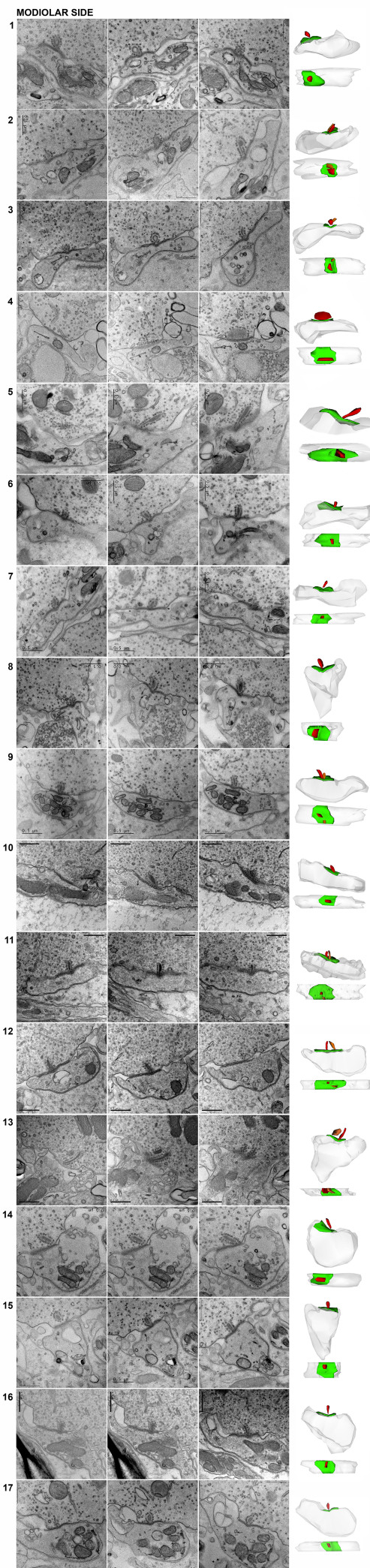


C Data from 3D serial sections

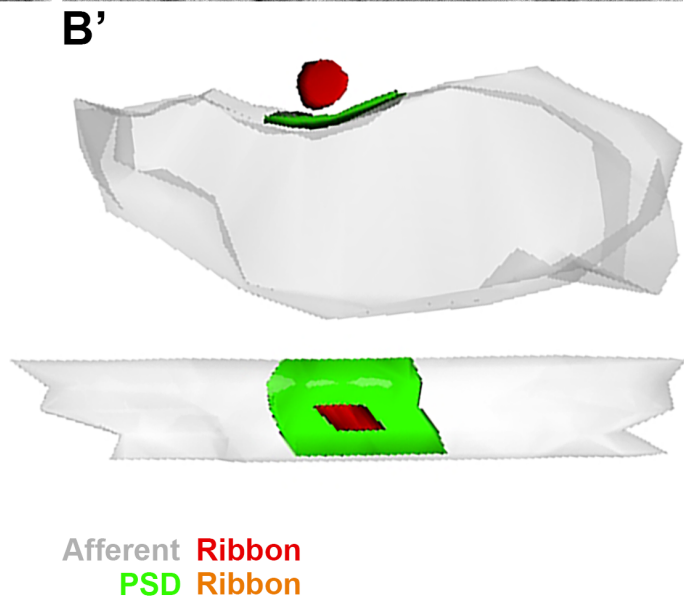
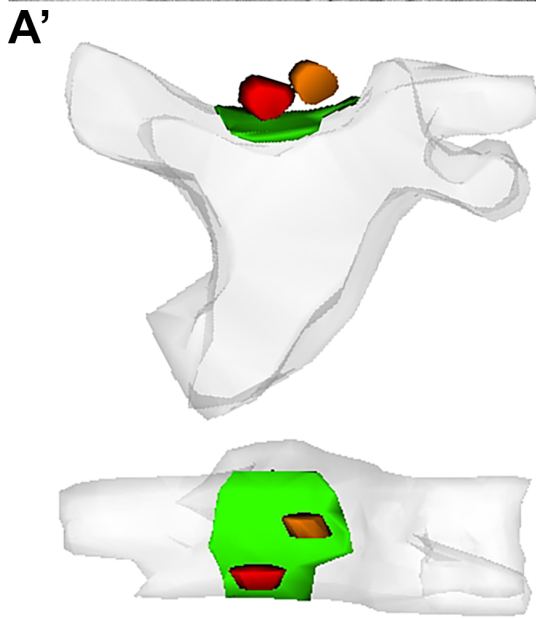
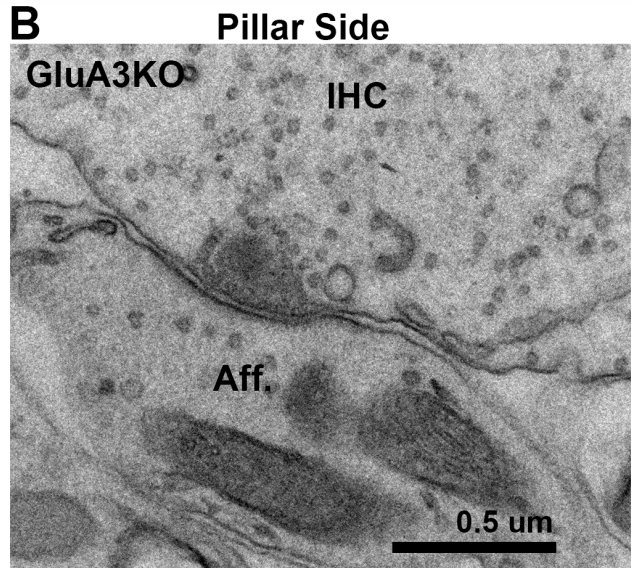
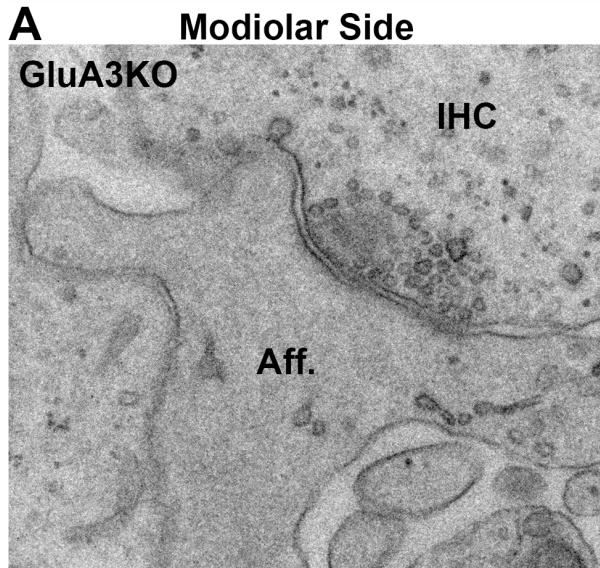


D Data from single ultrathin sections

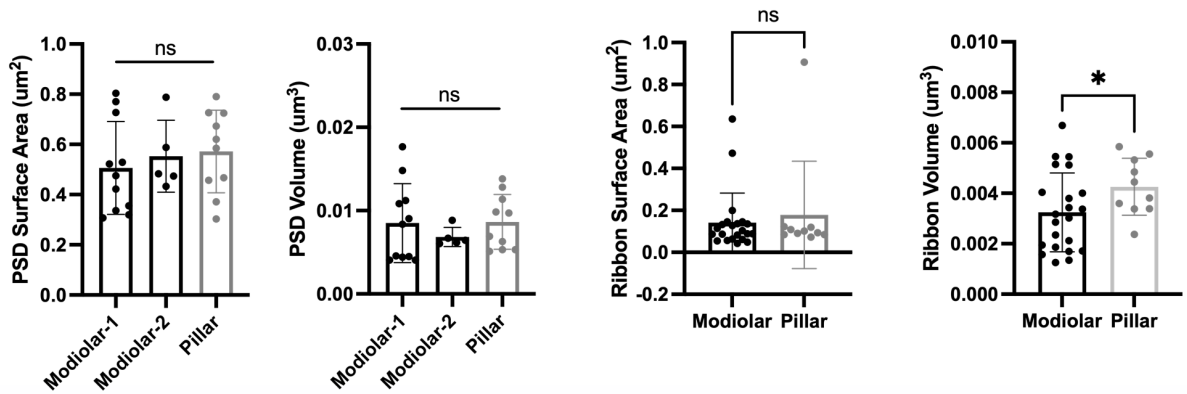




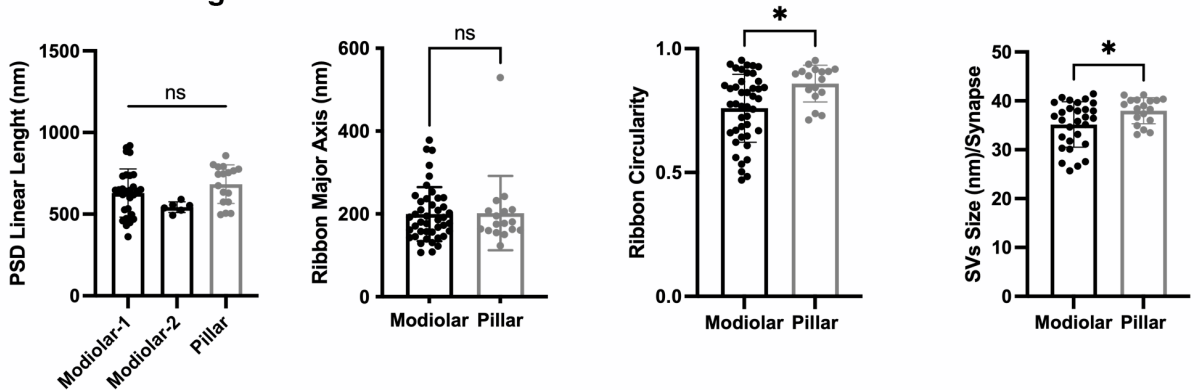
WILD TYPE

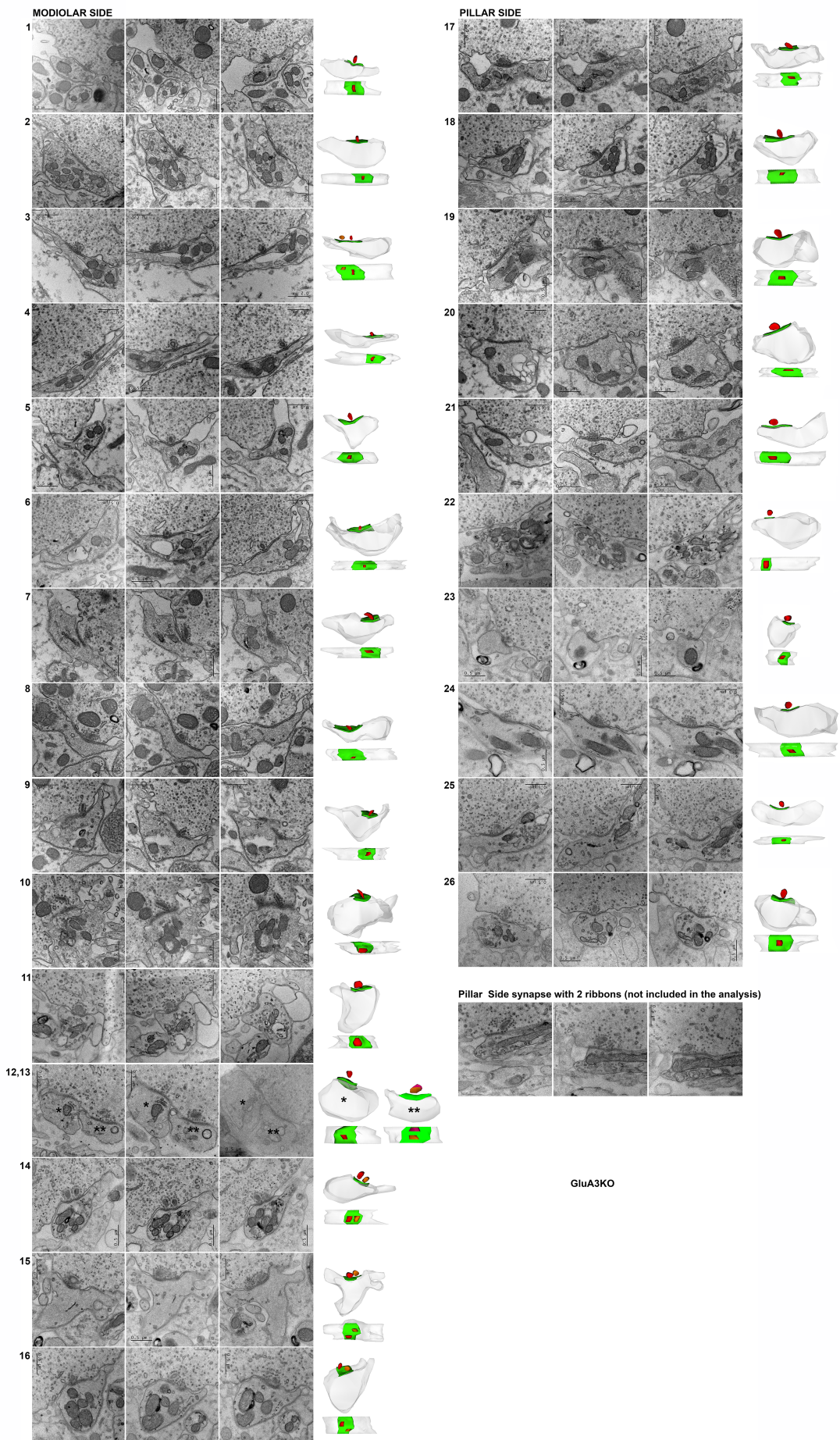


C Data from 3D reconstructions

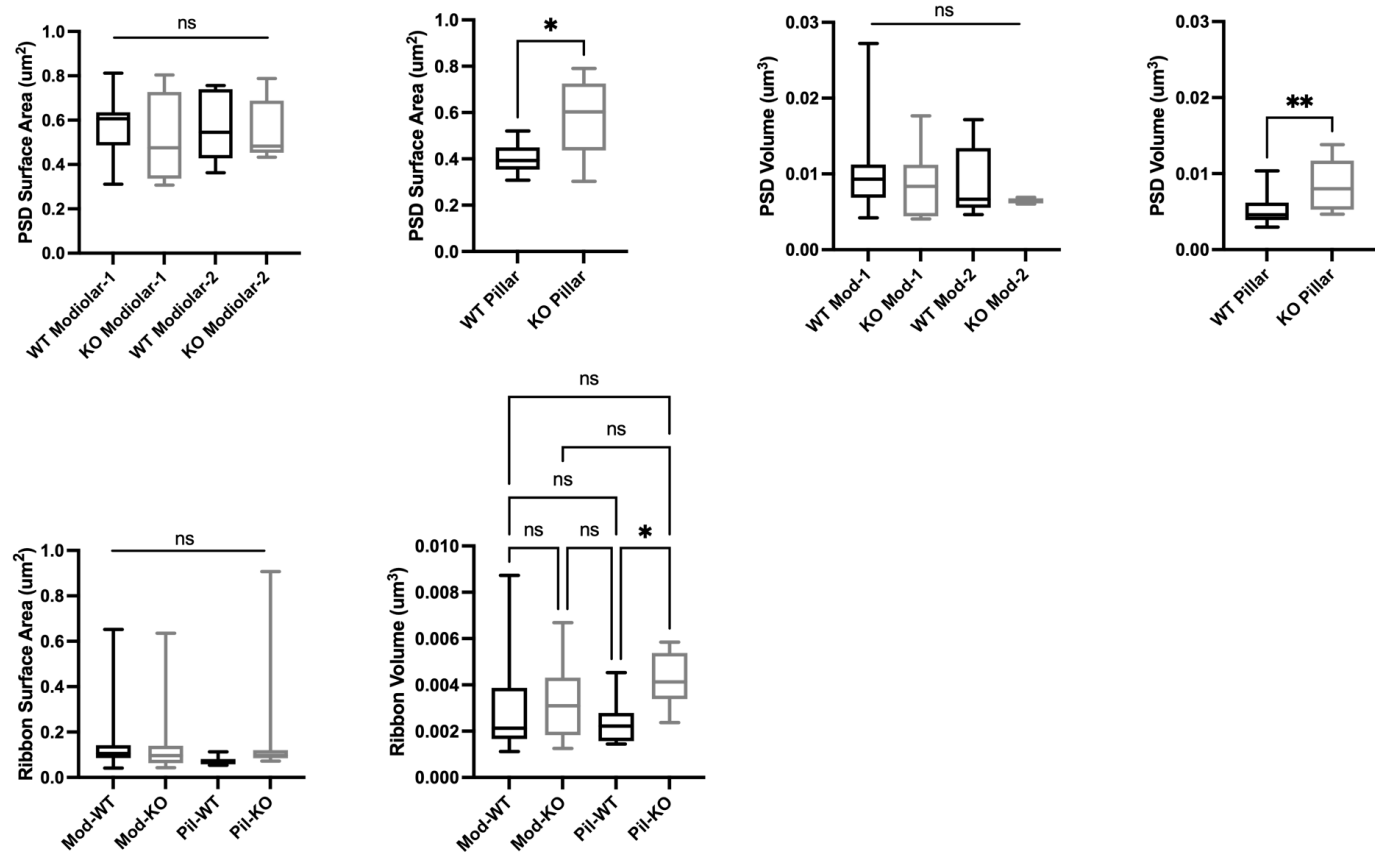


D Data from single ultrathin sections

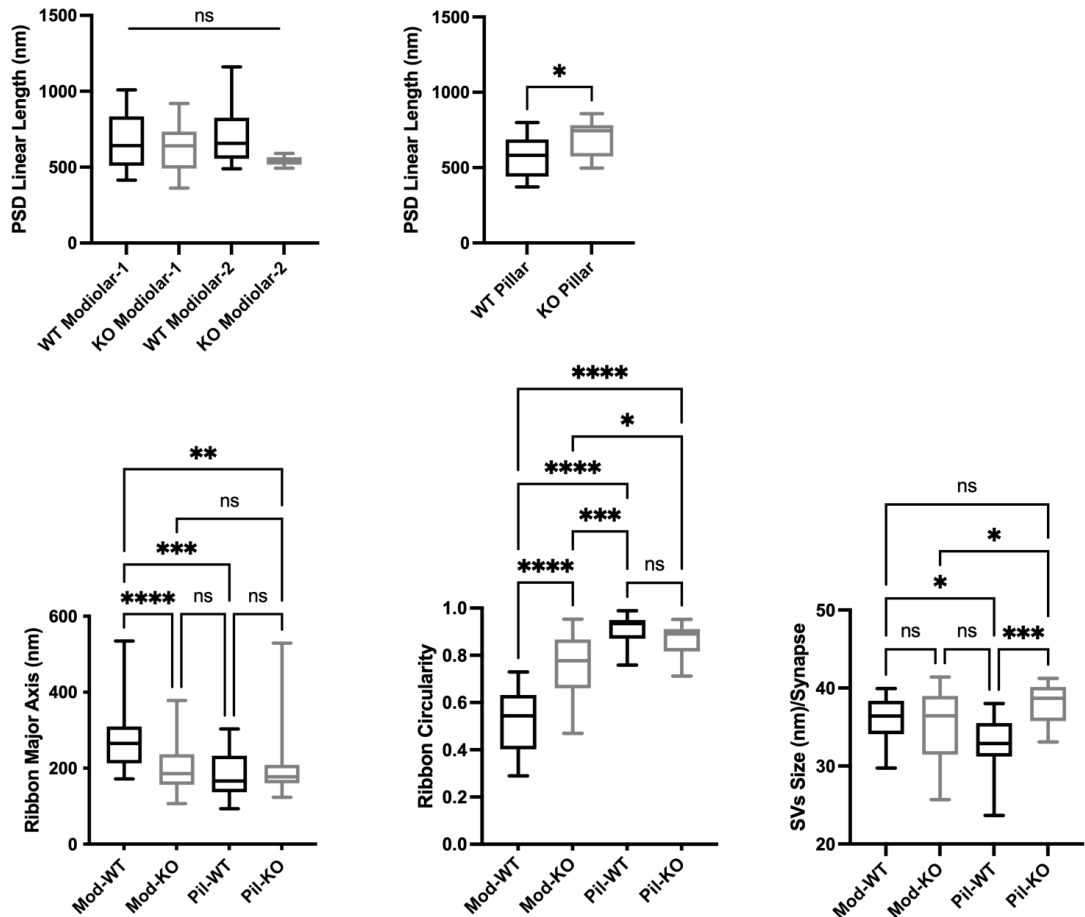




A Data from 3D reconstructions



B Data from single ultrathin sections



A

CtBP2 GluA2 GluA4

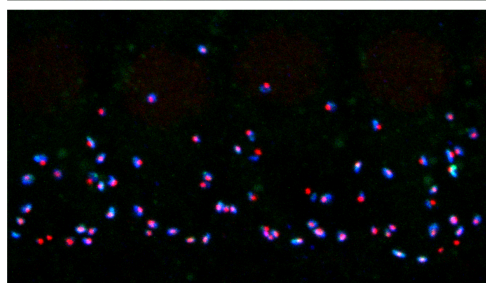
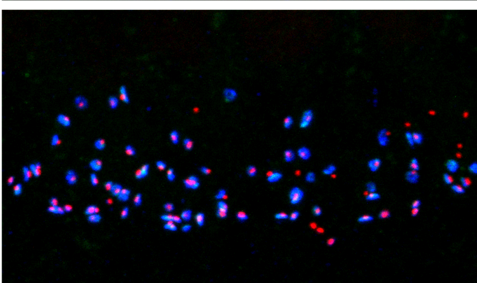
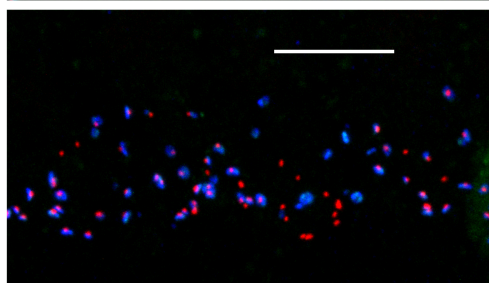
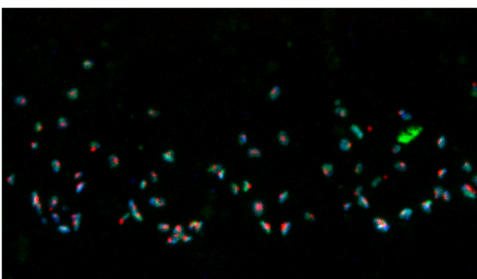
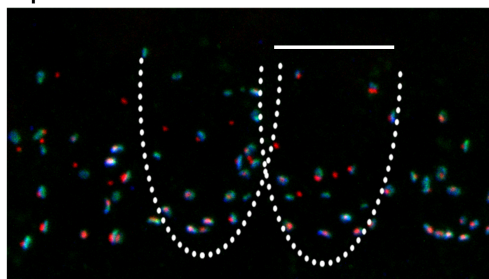
GluA3 WT

GluA3 KO

apical cochlea

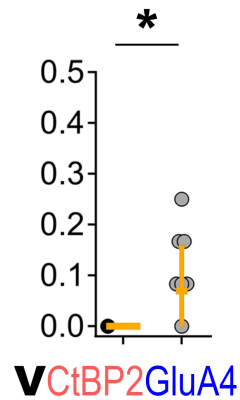
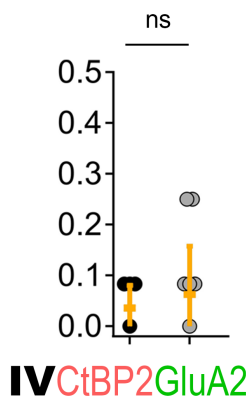
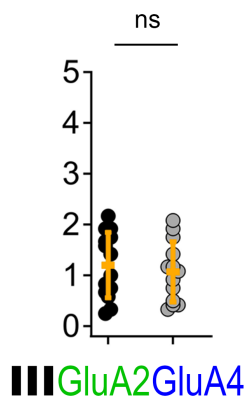
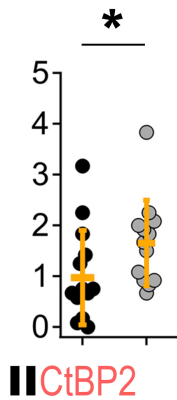
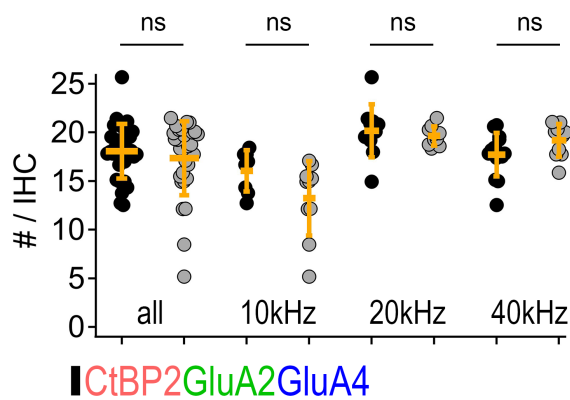
mid-cochlea

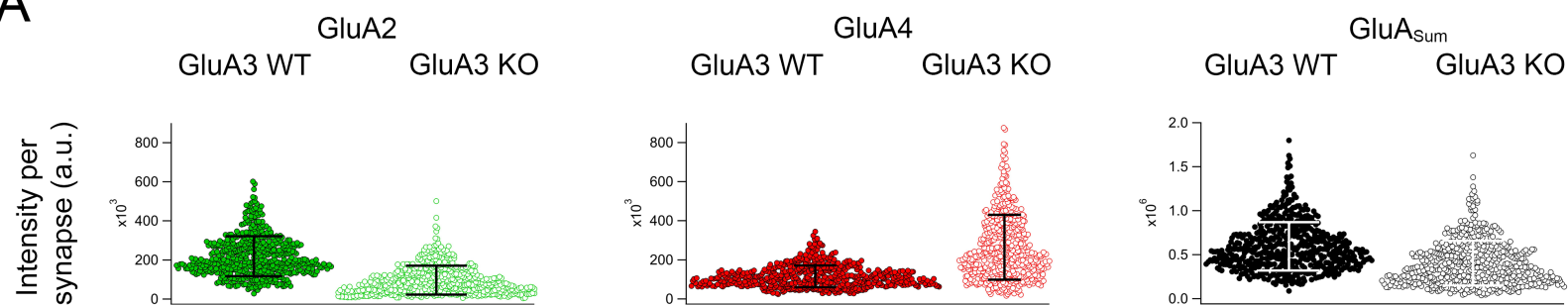
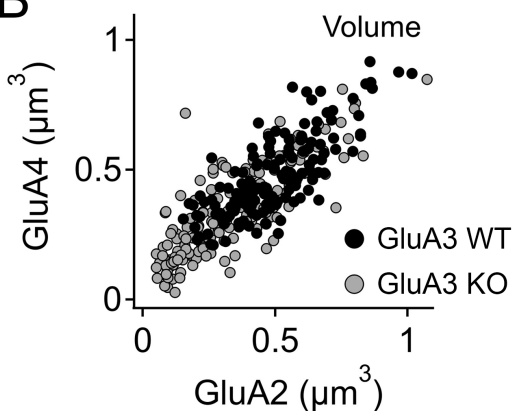
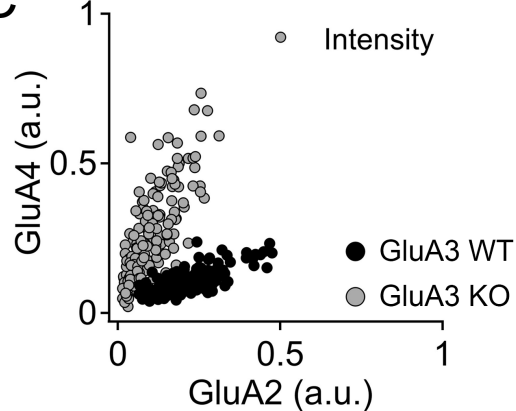
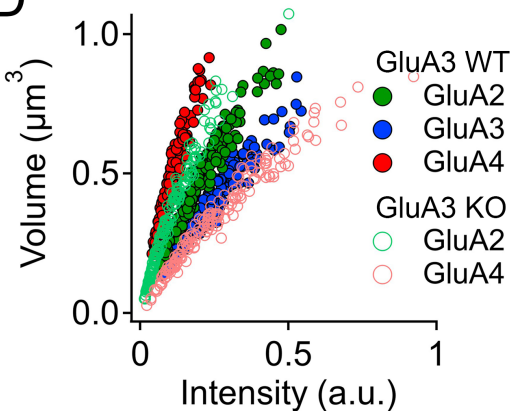
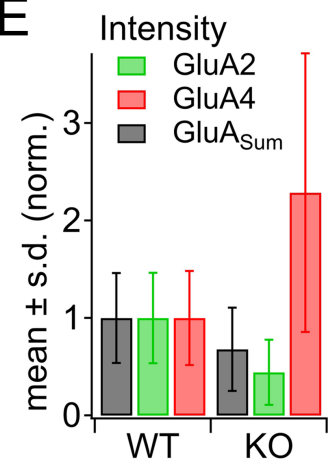
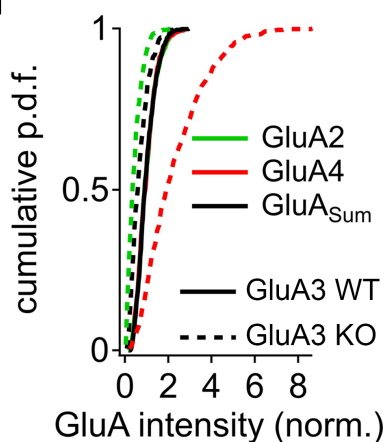
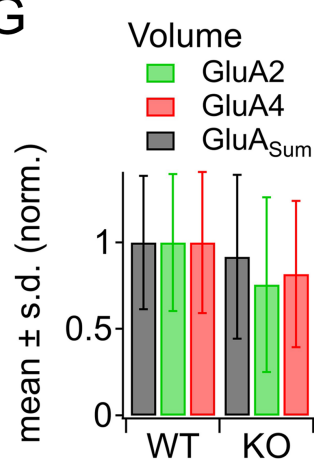
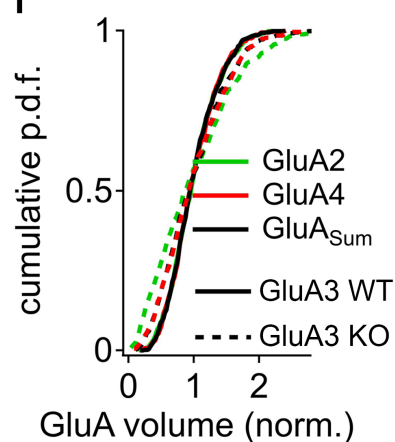
basal cochlea



B

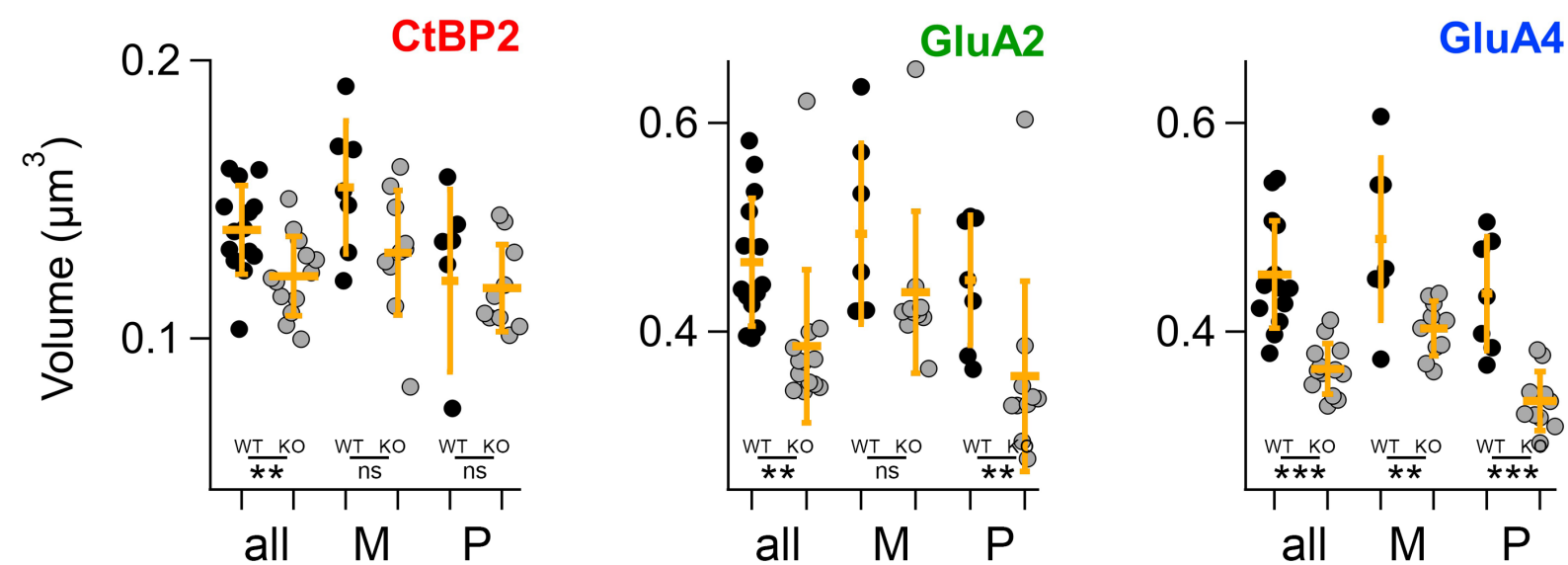
• GluA3 WT vs. • GluA3 KO



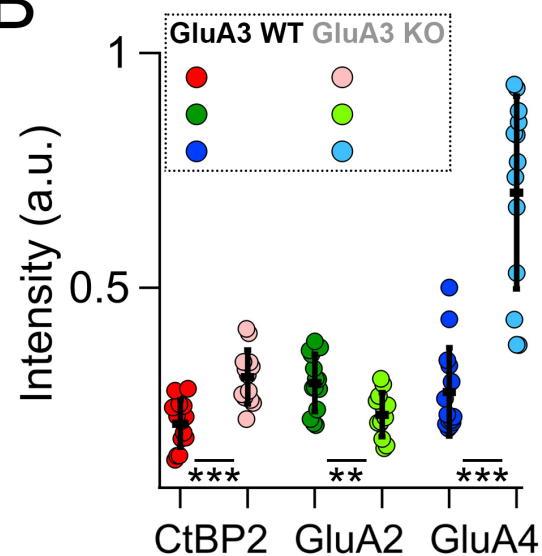
A**B****C****D****E****F****G****H**

A

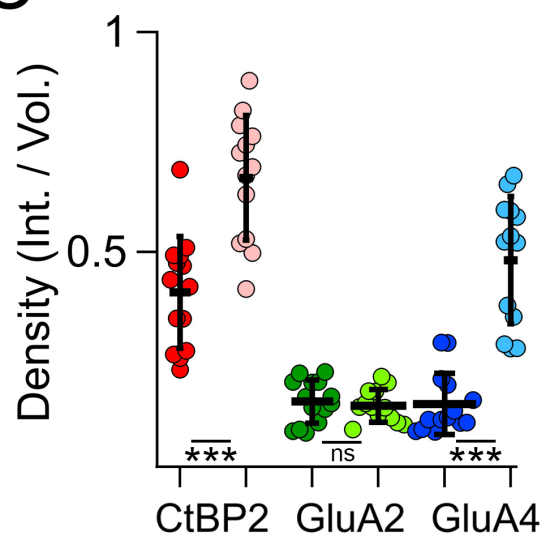
• **GluA3 WT** vs. • **GluA3 KO**



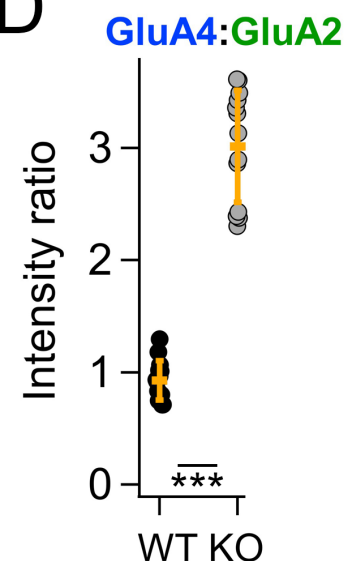
B



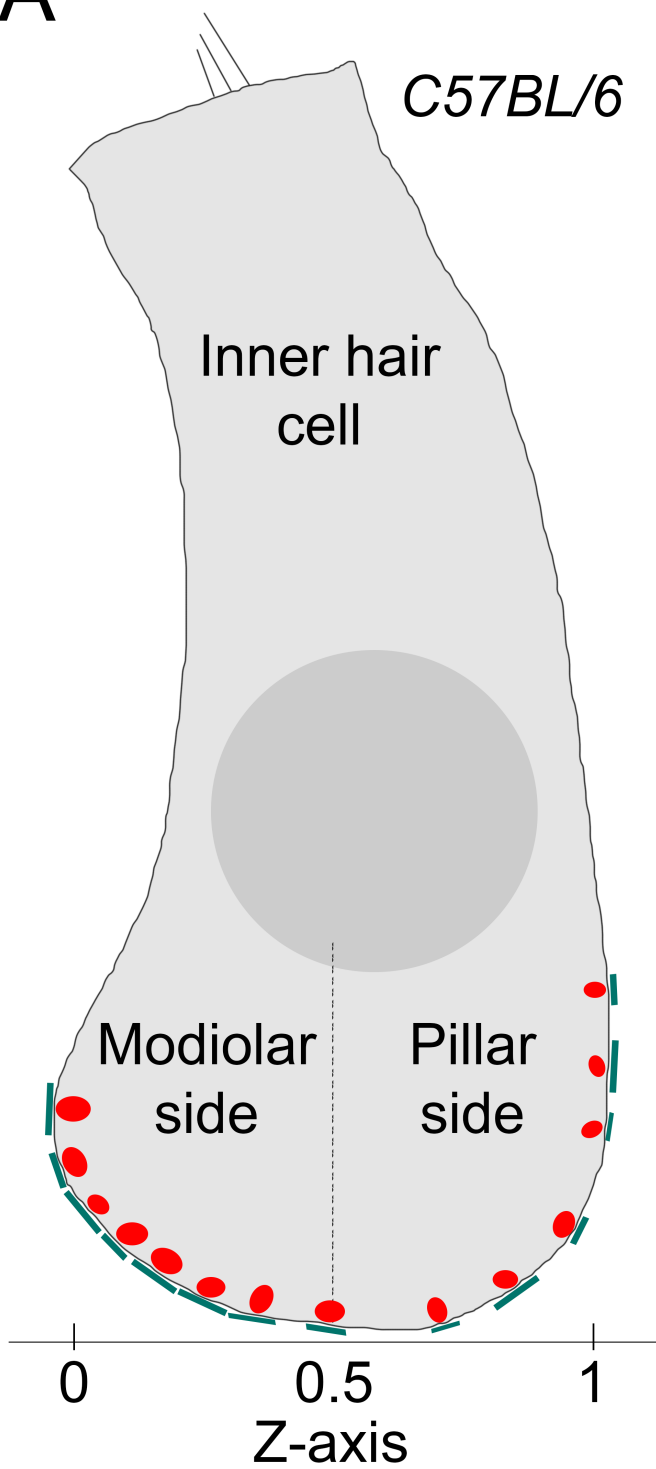
C



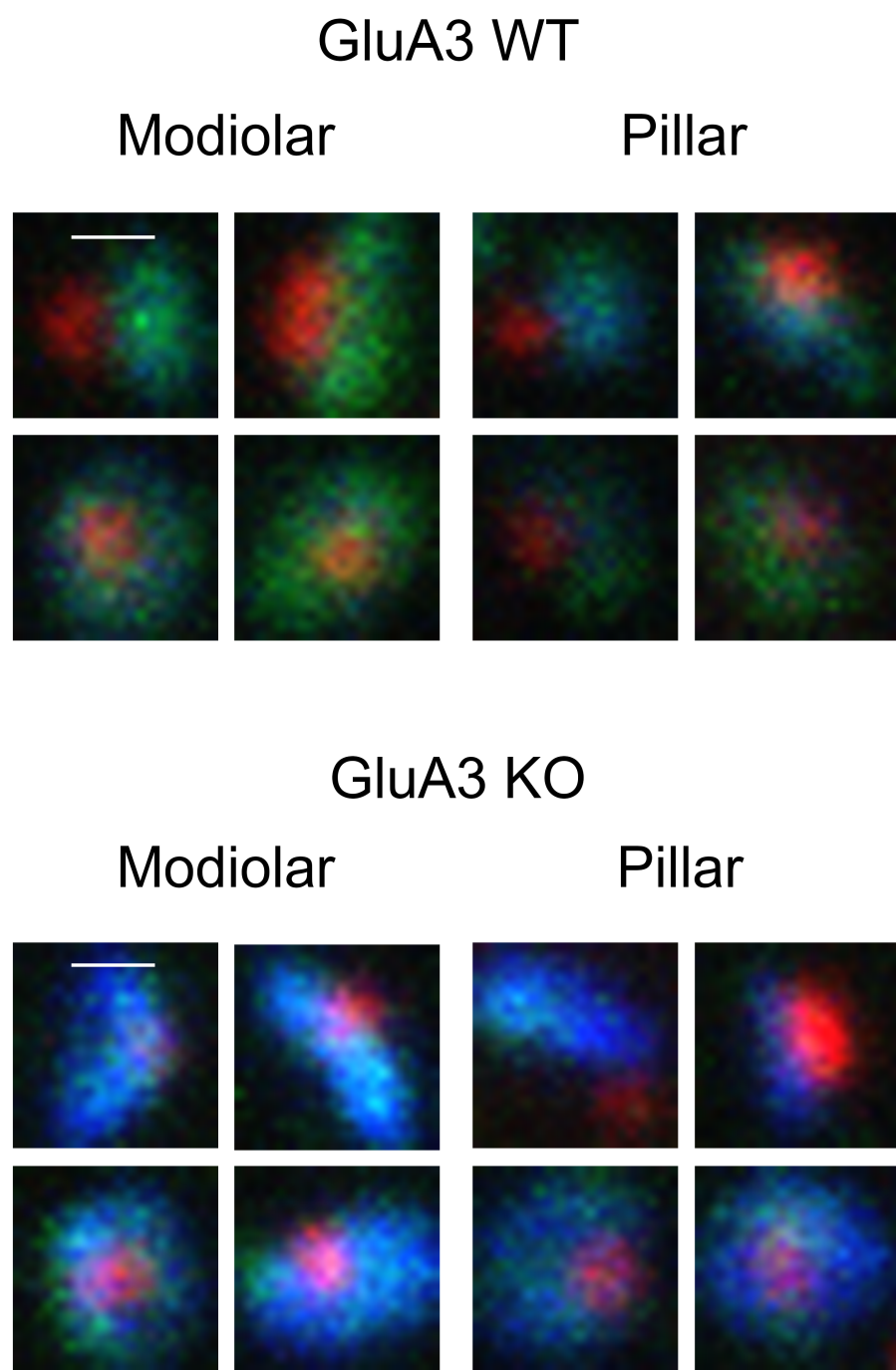
D

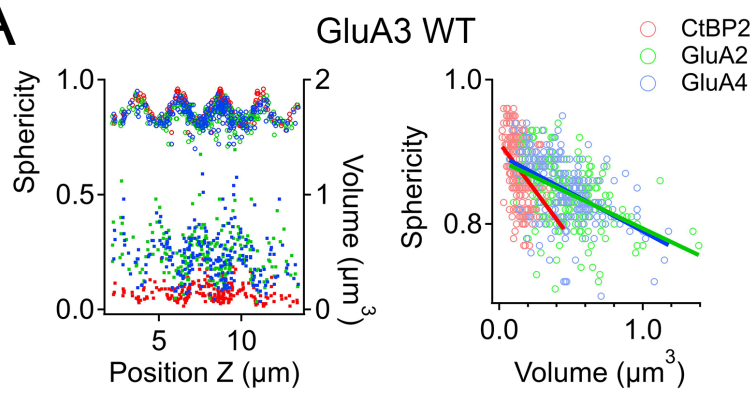
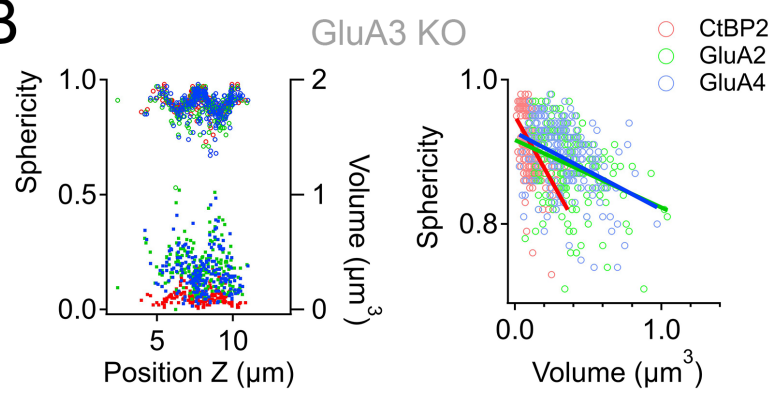
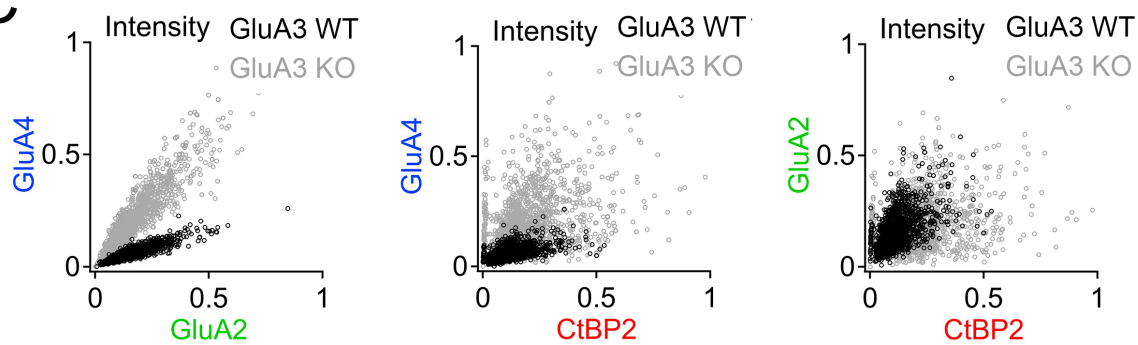


A



B



A**B****C****D**